Article

A probabilistic histological atlas of the human brain for MRI segmentation

https://doi.org/10.1038/s41586-025-09708-2

Received: 7 February 2024

Accepted: 6 October 2025

Published online: 5 November 2025

Open access

Check for updates

Adrià Casamitjana[1,2], Matteo Mancini[1,3,4], Eleanor Robinson[1], Loïc Peter[1], Roberto Annunziata[1], Juri Althonayan[1], Shauna Crampsie[1], Emily Blackburn[1], Benjamin Billot[1,5], Alessia Atzeni[1], Oula Puonti[6,7], Yaël Balbastre[1,7], Peter Schmidt[8], James Hughes[8], Jean C. Augustinack[7], Brian L. Edlow[7,9], Lilla Zöllei[7], David L. Thomas[10,11], Dorit Kliemann[12,13], Martina Bocchetta[10,14], Catherine Strand[15], Janice L. Holton[15], Zane Jaunmuktane[15] & Juan Eugenio Iglesias[1,5,7]✉

In human neuroimaging, brain atlases are essential for segmenting regions of interest (ROIs) and comparing subjects in a common coordinate frame. State-of-the-art atlases derived from histology[1–3] provide exquisite three-dimensional cytoarchitectural maps but lack probabilistic labels throughout the whole brain: that is, the likelihood of each location belonging to a given ROI. Here we present NextBrain, a probabilistic histological atlas of the whole human brain. We developed artificial intelligence-enabled methods to align roughly 10,000 histological sections from five whole brain hemispheres into three-dimensional volumes and to produce delineations for 333 ROIs on these sections. We also created a companion Bayesian tool for automatic segmentation of these ROIs in magnetic resonance imaging (MRI) scans. We showcase two applications of the atlas: segmentation of ultra-high-resolution ex vivo MRI and volumetric analysis of Alzheimer's disease using in vivo MRI. We publicly release raw and aligned data, an online visualization tool, the atlas, the segmentation tool, and ground truth delineations for a high-resolution ex vivo hemisphere used in validation. By enabling researchers worldwide to automatically analyse brain MRIs at a higher level of granularity, NextBrain holds promise to increase the specificity of findings and accelerate our quest to understand the human brain in health and disease.

MRI enables three-dimensional (3D) imaging of the human brain in vivo with millimetre resolution. Neuroimaging packages like FreeSurfer[4], FSL[5] and SPM[6] enable large-scale studies with thousands of MRI scans. A core component of these packages is digital atlases: reference 3D brain images that comprise image intensities, neuroanatomical labels or both. (We note that the cerebral cortex is often modelled with specific atlases defined on surface coordinate systems rather than 3D images.) Atlases enable comparison of different subjects in a common coordinate frame (CCF). When they include neuroanatomical labels, atlases also provide previous spatial information for analyses such as automated image segmentation[7].

Most volumetric atlases are built by averaging in vivo MRI scans from many subjects. However, their resolution (roughly 1 mm) is insufficient to study brain subregions with different function and connectivity[8]. Ex vivo MRI yields roughly 100-µm resolution[9–12] but still fails to visualize cytoarchitecture. Histology is a microscopic modality that addresses this issue. Earlier versions of histological atlases were printed and comprised a small number of sections[13]. Subsequent efforts combined serial histology with image registration to produce 3D histological atlases[14]. These were mapped to in vivo scans of living subjects by means of intermediate 3D MRI templates (for example, the Montreal Neurological Institute (MNI) atlas[15]) or directly with Bayesian methods.

Earlier 3D histological atlases modelled only one brain region (for example, thalamus, basal ganglia[16–18]). More recent efforts targeted the whole brain. BigBrain[1] comprises more than 7,000 histological sections of a single brain, but without labels. Its follow-up, Julich-Brain[2], aggregates data from 23 individuals, with community-sourced labels for 248 cytoarchitectonic areas mapped to MNI space—albeit with limited accuracy and only partial subcortical labelling[19]. The Allen reference brain[3] has comprehensive anatomical annotations but only on a sparse set of sections of a single specimen. The Allen MNI template is labelling of the MNI atlas with the Allen anatomical protocol, but with

[1]Department of Medical Physics and Biomedical Engineering, University College London, London, UK. [2]Research Institute of Computer Vision and Robotics, University of Girona, Girona, Spain. [3]Enrico Fermi Research Center, Rome, Italy. [4]Cardiff University Brain Research Imaging Centre, Cardiff University, Cardiff, UK. [5]Computer Science and Artificial Intelligence Laboratory, Massachusetts Institute of Technology, Cambridge, MA, USA. [6]Danish Research Centre for Magnetic Resonance, Centre for Functional and Diagnostic Imaging and Research, Copenhagen University Hospital - Amager and Hvidovre, Copenhagen, Denmark. [7]Athinoula A. Martinos Center for Biomedical Imaging, Massachusetts General Hospital and Harvard Medical School, Boston, MA, USA. [8]Advanced Research Computing Centre, University College London, London, UK. [9]Center for Neurotechnology and Neurorecovery, Department of Neurology, Massachusetts General Hospital and Harvard Medical School, Boston, MA, USA. [10]Dementia Research Centre, Department of Neurodegenerative Disease, UCL Queen Square Institute of Neurology, University College London, London, UK. [11]Neuroradiological Academic Unit, Department of Brain Repair and Rehabilitation, UCL Queen Square Institute of Neurology, University College London, London, UK. [12]Department of Psychological and Brain Sciences, The University of Iowa, Iowa City, IA, USA. [13]Department of Psychiatry, The University of Iowa, Iowa City, IA, USA. [14]Centre for Cognitive and Clinical Neuroscience, Division of Psychology, Department of Life Sciences, College of Health, Medicine and Life Sciences, Brunel University London, London, UK. [15]Queen Square Brain Bank for Neurological Disorders, Department of Clinical and Movement Neurosciences, UCL Queen Square Institute of Neurology, University College London, London, UK. ✉e-mail: jiglesiasgonzalez@mgh.harvard.edu

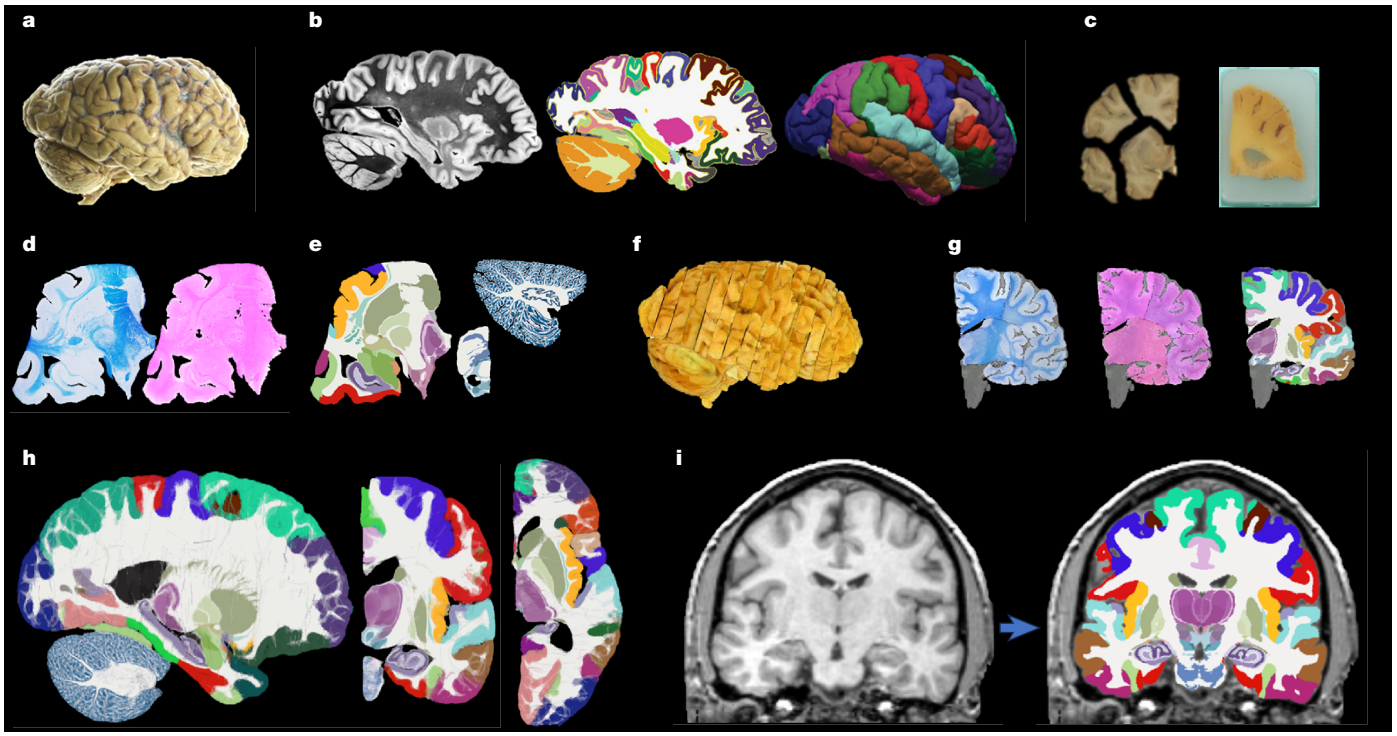

Fig. 1 | NextBrain workflow. a, Photograph of formalin-fixed hemisphere (lateral view). **b**, High-resolution (400 µm) ex vivo MRI scan, FreeSurfer segmentation and extracted pial surface (parcellated with FreeSurfer). Left, sagittal slice of MRI. Centre, corresponding FreeSurfer segmentation. Right, 3D rendering of reconstructed and parcellated pial surface. **c**, Tissue slabs and blocks, before and after paraffin embedding. Left, blocked coronal slice of the cerebrum. Right, blockface photo of a cerebral block. **d**, Histology: coronal section of cerebrum stained with LFB (left) and H&E (right). **e**, Artificial-intelligence-assisted labelling of 333 ROIs on LFB. Left, cerebrum; centre, brainstem; right, cerebellum[28]. **f**, Initialization of affine alignment of tissue blocks using a custom registration algorithm that minimizes overlap and gaps between blocks. **g**, Refinement of registration with histology and nonlinear transform[24,25]. Reconstructed coronal slice of LFB (left), H&E (middle) and labels (right), overlaid on MRI, after nonlinear registration with artificial intelligence and robust Bayesian refinement. **h**, Orthogonal slices of our 3D probabilistic atlas. Left, sagittal; middle, coronal; right, axial. Each voxel is painted with a linear combination the colours of each label, multiplied by their probabilities. **i**, Automated Bayesian segmentation of an in vivo scan into 333 ROIs using the atlas. The atlas can also be used for segmenting ex vivo MRI and as CCF for population analyses.

a fraction of the labels and less accurate delineations owing to limited resolution and contrast. The Ahead brains[20] comprise quantitative MRI and registered 3D histology for two separate specimens, but labels are available for only a few dozen structures and are automated rather than manual. Further details on these atlases can be found in the 'Extended Introduction' in the Supplementary Information.

Although existing histological atlases provide exquisite 3D cytoarchitectural maps and some degree of MRI–histology integration, there are at present neither (1) datasets with densely labelled 3D histology of the whole brain nor (2) probabilistic atlases built from such datasets, which would enable analyses such as Bayesian segmentation or CCF mapping of the whole brain.

To address these issues, we present NextBrain, a densely labelled probabilistic atlas of the human brain built from histology images. We used custom artificial-intelligence-enabled registration and segmentation methods to assemble 3D reconstructions of multimodal serial histology of five human half brains, semi-automatically segment them into 333 ROIs and average the labels into the probabilistic atlas. NextBrain is open source and includes the atlas, a companion Bayesian segmentation method, the data (with an online visualization tool) and ground truth delineations for a 100-µm isotropic ex vivo scan[12].

Densely labelled 3D histology of five human hemispheres

The NextBrain workflow is summarized in Fig. 1 and detailed in Methods. The first result of the pipeline (Fig. 1a–g) is a multimodal dataset with human hemispheres from five donors (three right, two left), including half cerebellum and brainstem. Each of the five cases comprises accurately aligned high-resolution ex vivo MRI, serial histology with hematoxylin and eosin (H&E) and Luxol fast blue (LFB) stains, and dense ground truth segmentations of 333 cortical and subcortical brain ROIs.

Aligning the histology of a case is analogous to solving a 2,000-piece jigsaw puzzle in 3D, with the ex vivo MRI as reference (similar to the image on the box cover), and with pieces that are deformed by sectioning and mounting on glass slides—with occasional tissue folding or tearing. This problem falls out of the scope of existing intermodality registration techniques[21], including slice-to-volume[22] and 3D histology reconstruction methods[14], which do not have to address the joint constraints of thousands of sections acquired in non-parallel planes as part of different blocks.

Instead, we solve this challenging problem with a custom, state-of-the-art image registration framework (Fig. 2), which includes three components specifically developed for this project: (1) a differentiable regularizer that minimizes overlap of different blocks and gaps in between[23], (2) an artificial intelligence registration method that uses contrastive learning to provide highly accurate alignment of corresponding brain tissue across MRI and histology[24] and (3) a Bayesian refinement technique based on Lie algebra that guarantees the 3D smoothness of the reconstruction across modalities, even in the presence of outliers due to tissue folding and tearing[25]. We note that this is an evolution of our previously presented pipeline[26], which incorporates the aforementioned contrastive artificial intelligence method and jointly optimizes the affine and nonlinear transforms to achieve a 32% reduction in registration error (details below).

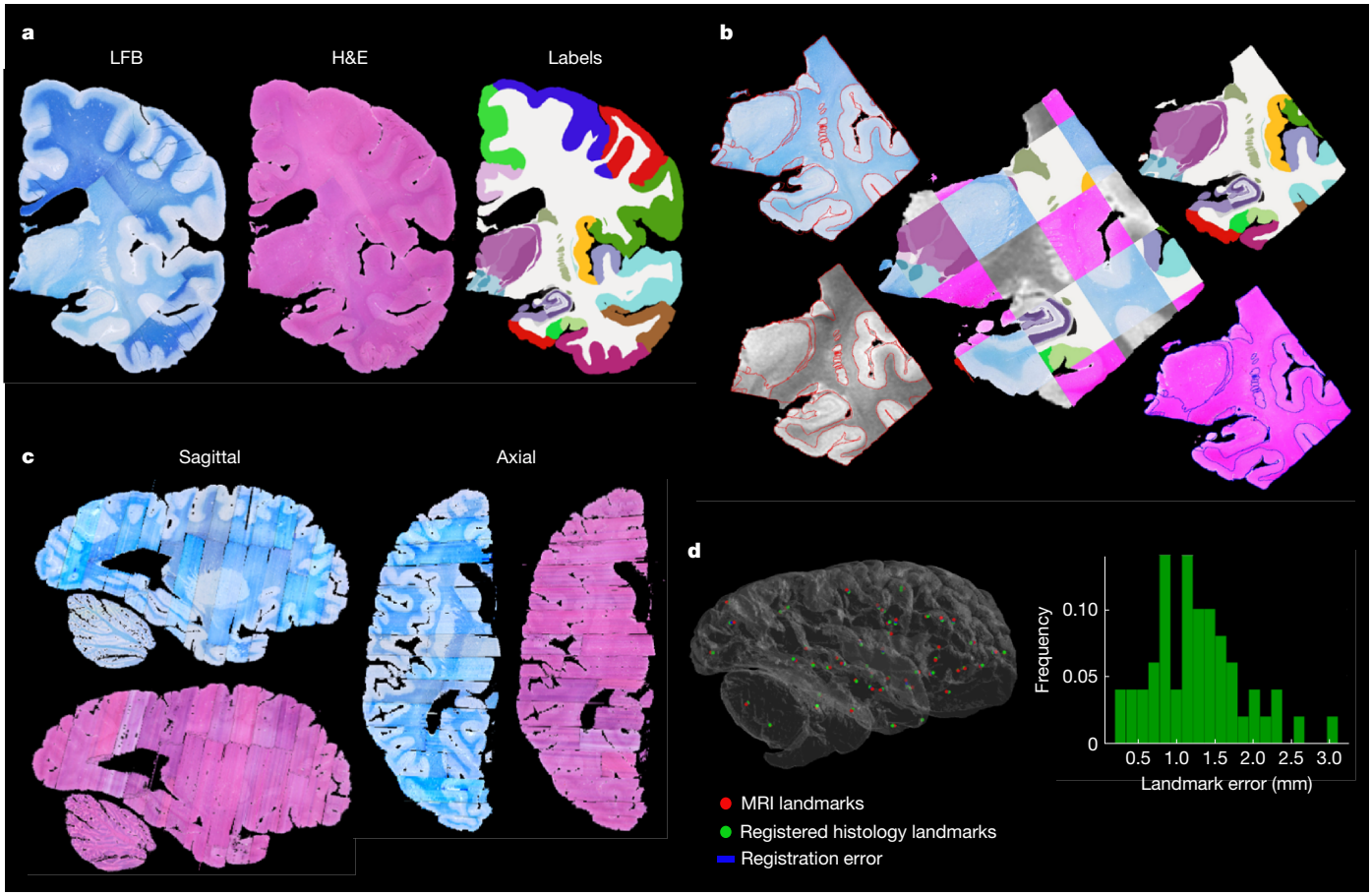

Fig. 2 | 3D histology reconstruction of Case 1. a, Coronal slice of 3D reconstruction; boundaries between blocks are noticeable from uneven staining. Joint registration minimizes overlap and and gaps between blocks (this reconstructed slice comprises four different blocks). **b**, Accurate intermodality registration with artificial intelligence techniques. Registered MRI, LFB and H&E histology of a block, with tissue boundaries (traced on LFB) overlaid. **c**, Orthogonal view of reconstruction, which is smooth thanks to the Bayesian refinement and avoids gaps and overlaps thanks to the regularizer. **d**, Visualization of 3D landmark registration errors for Case 1. Left, visualization of landmarks. Right, histogram, mean and s.d. of error magnitude for this case, compared with our previous pipeline. Error (mean ± s.d.): 1.27 ± 0.59 mm. Error[26]: 1.42 ± 0.72 mm. See Table 1 and Extended Data Figs. 1, 2, 3 and 4 for results on the other cases.

Qualitatively, it is apparent from Fig. 2 that a very high level of accuracy is achieved for the spatial alignment, despite the non-parallel sections and distortions in the raw data. The regularizer effectively aligns the block boundaries in 3D without gaps or overlap (Fig. 2a–c), with minor discontinuities across blocks (for example, in the temporal lobe). When the segmentations of different blocks are combined (Fig. 2a, right), the result is a smooth mosaic of ROI labels.

The artificial-intelligence-enabled registration across MRI and histological stains is exemplified in Fig. 2b. Overlaying the main ROI contours on the different modalities shows the highly accurate alignment of the three modalities (MRI, H&E, LFB) even in convoluted regions of the cortex and the basal ganglia. The mosaic of modalities also highlights the accurate alignment at the substructural level: for example, subregions of the hippocampus.

Figure 2c shows the 3D reconstruction in orientations orthogonal to the main plane of sectioning (coronal). This illustrates not only the lack of gaps and overlaps between blocks but also the smoothness that is achieved within blocks. This is thanks to the Bayesian refinement algorithm, which combines the best features of methods that (1) align each section independently (high fidelity to the reference, but jagged reconstructions) and (2) those that align sections to their neighbours (smooth reconstructions, but with a 'banana effect': that is, straightening of curved structures).

To quantitatively evaluate the 3D reconstruction accuracy, we used 250 manually placed pairs of landmarks to compute registration errors (50 landmarks per case); landmarks are known to be a better proxy for registration error than similarity of label overlap metrics[27]. Table 1 displays means and standard deviations of the registration error for each of the five cases, comparing our method with our previous pipeline[26]. Histograms and 3D visualizations of the errors for individual cases can be found in Fig. 2d and in Extended Data Figs. 1d, 2d, 3d and 4d. Our method yields an average error of 0.99 mm (s.d., 0.51 mm; standard error, 0.03 mm), which is a considerable reduction with respect to ref. 26, which yielded 1.44 mm (s.d., 0.58 mm; standard error, 0.04 mm). The difference between the two methods is strongly significant: *P* values computed with a non-parametric paired Wilcoxon test were under 0.001 for all cases, and the *P* value for all 250 landmarks was $P < 10^{-21}$; see details in Table 1. The spatial distribution of the error is further visualized with kernel regression in Extended Data Fig. 5, which shows that this distribution is fairly uniform: that is, there is no obvious consistent pattern across cases.

Our pipeline is widely applicable as it produces accurate 3D reconstructions from blocked tissue in standard-sized cassettes, sectioned with a standard microtome. The computer code and aligned dataset are freely available in our public repository. For educational and data inspection purposes, we have built an online visualization tool for the multimodality data, which is available at https://github-pages.ucl.ac.uk/BrainAtlas.

Supplementary Video 1 illustrates the aligned data, which include (1) MRI at 400-µm isotropic resolution, (2) aligned H&E and LFB

Table 1 | 3D registration errors (in millimetres) for our method versus ref. 26

Case	Error (μ±σ), our method	Error (μ±σ), previous method[26]	*P* value (paired Wilcoxon)
Case 1	1.27±0.59	1.42±0.72	8.8×10^{-4}
Case 2	0.98±0.55	1.49±0.65	5.6×10^{-5}
Case 3	0.80±0.32	1.41±0.68	2.0×10^{-7}
Case 4	1.05±0.50	1.49±0.70	1.5×10^{-4}
Case 5	0.83±0.57	1.39±0.66	6.2×10^{-7}
All combined	0.99±0.51	1.44±0.68	4.0×10^{-22}

We used $N=50$ for each case (250 all combined). Statistical significance is computed using a two-sided Wilcoxon test.

histology digitized at 4-μm resolution (with 250-μm or 500-μm spacing, depending on the brain location) and (3) ROI segmentations, obtained with a semi-automated artificial intelligence method[28]. The ROIs comprise 34 cortical labels (following the Desikan–Killiany atlas[29]) and 299 subcortical labels (following different atlases for different brain regions; Methods and Supplementary Information). This public dataset enables researchers worldwide to conduct their own studies not only in 3D histology reconstruction but also other fields, such as high-resolution segmentation of MRI or histology[30], MRI-to-histology and histological stain-to-stain image translation[31], deriving MRI signal models from histology[32] and many others.

A next-generation probabilistic atlas of the human brain

The labels from the five human hemispheres were coregistered and merged into a probabilistic atlas. This was achieved with a method that alternately registers the volumes to the estimate of the template and updates the template by means of averaging[33]. The registration method is diffeomorphic[34] to ensure preservation of the neuroanatomic topology (for example, ROIs do not split or disappear in the deformation process). Crucially, we use an initialization based on the MNI template, which serves two important purposes: preventing biases towards any of the cases (which would happen if we initialized with one of them) and 'centring' our atlas on a well-established CCF computed from 305 subjects, which largely mitigates our relatively low number of cases. Because the MNI template is a greyscale volume, the first iteration of atlas building uses registrations computed with the ex vivo MRI scans. Subsequent iterations register labels directly with a metric based on the probability of the discrete labels according to the atlas[33].

Figure 3 shows close-ups of orthogonal slices of the atlas, which model voxel-wide probabilities for the 333 ROIs on a 0.2-mm isotropic grid. The resolution and detail of the atlas represent a substantial advance with respect to the SAMSEG atlas[35] now in FreeSurfer (Fig. 3a). SAMSEG models 13 brain ROIs at 1-mm resolution and is a highly detailed probabilistic atlas that covers all brain regions. The figure also shows roughly corresponding slices of the manual labelling of the MNI atlas with the simplified Allen protocol[3]. Compared with NextBrain, this labelling is not probabilistic and does not include many histological boundaries that are invisible on the MNI template (for example, hippocampal subregions, in violet). For this reason, it only has 138 ROIs—whereas NextBrain has 333.

A comparison between labelled sections of the printed atlas by ref. 13 and roughly equivalent sections of the Allen reference brain and NextBrain is included in the Supplementary Information. The agreement between the three atlases is generally good, especially for the outer boundaries of the whole structures: for example, the whole hippocampus, amygdala or thalamus. Mild differences can be found in the delineation of substructures, both cortical and subcortical (for example, subdivision of the accumbens), mainly due to (1) the forced choice of applying arbitrary anatomical criteria in both atlases because of lack of contrast in smaller regions, (2) different anatomical definitions and (3) the probabilistic nature of NextBrain. We emphasize that these differences are not exclusive to NextBrain, as they are also present between Mai–Paxinos and Allen.

Close-ups of NextBrain slices centred on representative brain regions are shown in Fig. 3b, with boundaries between the ROIs (computed from the maximum likelihood segmentation) overlaid in red. These highlight the anatomical granularity of the new atlas, with dozens of subregions for areas such as the thalamus, hippocampus, amygdala, midbrain and so on. An overview of the complete atlas is shown in Supplementary Video 2, which illustrates the atlas construction procedure and flies through all the slices in axial, coronal and sagittal view.

The probabilistic atlas is freely available as part of our segmentation module distributed with FreeSurfer. The maximum likelihood and colour-coded probabilistic maps (as in Fig. 3) can also be downloaded separately from our public repository for quick inspection and educational purposes. Developers of neuroimaging methods can freely capitalize on this resource, for example, by extending the atlas through combination with other atlases or manually tracing new labels; or by designing their own segmentation methods using the atlas. Neuroimaging researchers can use the atlas for fine-grained automated segmentation (as shown below) or as a highly detailed CCF for population analyses.

Segmentation of ultra-high-resolution ex vivo MRI

One of the new analyses that NextBrain enables is the automated fine-grained segmentation of ultra-high-resolution ex vivo MRI. Because motion is not a factor in ex vivo imaging, very long MRI scanning times can be used to acquire data at resolutions that are infeasible in vivo. One example is the publicly available 100-μm isotropic whole brain presented in ref. 12, which was acquired in a 100-hour session on a 7-T MRI scanner. Such datasets have huge potential in mesoscopic studies connecting microscopy with in vivo imaging[36].

Volumetric segmentation of ultra-high-resolution ex vivo MRI can be highly advantageous in neuroimaging in two different manners: first, by supplementing such scans (like the 100-micron brain) with neuroanatomical information that augments their value as atlases (for example, as CCFs or for segmentation purposes[37]); and second, by enabling analyses of ex vivo MRI datasets at scale (for example, volumetry or shape analysis).

Dense manual segmentation of these datasets is practically infeasible, as it entails manually tracing ROIs on over 1,000 slices. Moreover, one typically seeks to label these images at a higher level of detail than in vivo (that is, more ROIs of smaller sizes), which exacerbates the problem. One may use semi-automated methods like the artificial-intelligence-assisted technique we used in to build NextBrain (see the previous section), which limits the manual segmentation to one every N slices[28] ($N = 4$ in this work). However, such a strategy only ameliorates the problem to a certain degree, as tedious manual segmentation is still required for a significant fraction of slices.

A more appealing alternative is thus automated segmentation. However, existing approaches have limitations, as they either (1) were designed for 1-mm in vivo scans and do not capitalize on the increased resolution of ex vivo MRI[18,35] or (2) use neural networks trained with ex vivo scans but with a limited number of ROIs because of the immense labelling effort that is required to generate the training data[30].

This limitation is circumvented by NextBrain: as a probabilistic atlas of neuroanatomy, it can be combined with well-established Bayesian segmentation methods (which are adaptive to MRI contrast) to segment ultra-high-resolution ex vivo MRI scans into 333 ROIs. We have released in FreeSurfer an implementation that segments full brain scans in about 1 h, using a desktop equipped with a graphics processing unit.

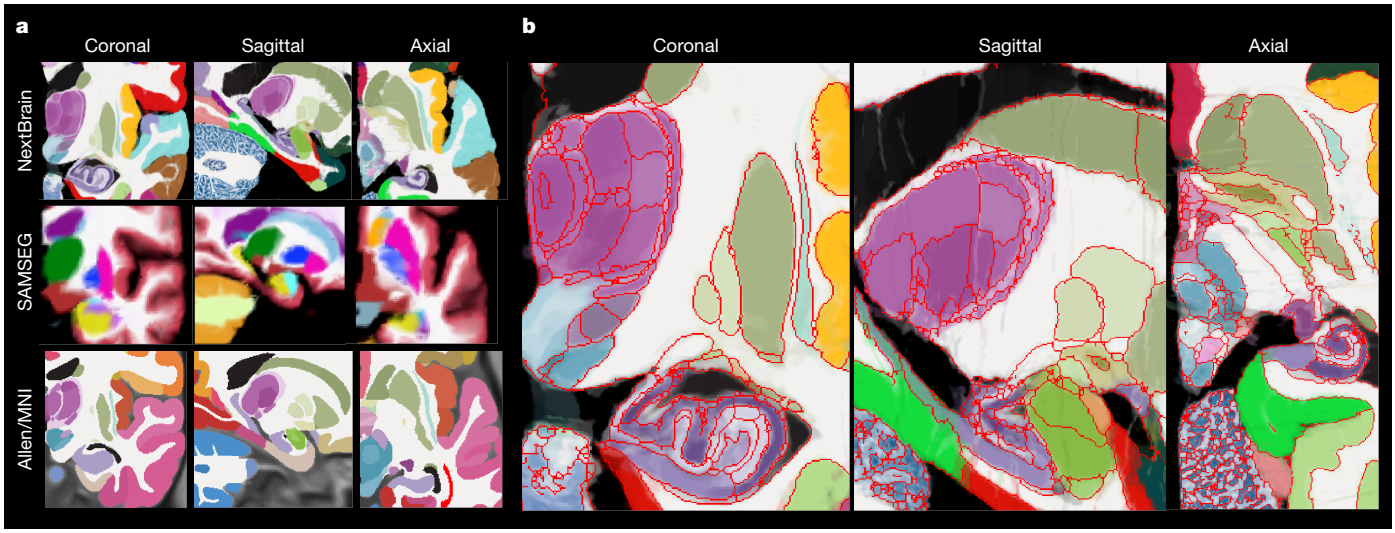

Fig. 3 | NextBrain probabilistic atlas. a, Comparison with whole brain atlases. Portions of the NextBrain probabilistic atlas (which has 333 ROIs), the SAMSEG atlas in FreeSurfer[35] (13 ROIs) and the manual labels of MNI based on the Allen atlas[3] (138 ROIs). **b**, Close-up of three orthogonal slices of NextBrain. The colour coding follows the convention of the Allen atlas[3], where the hue indicates the structure (for example, purple is thalamus, violet is hippocampus, green is amygdala) and the saturation is proportional to neuronal density. The colour of each voxel is a weighted sum of the colour corresponding to the ROIs, weighted by the corresponding probabilities at that voxel. The red lines separate ROIs on the basis of the most probable label at each voxel, thus highlighting boundaries between ROIs of similar colour; we note that the jagged boundaries are a common discretization artefact of probabilistic atlases in regions where two or more labels mix continuously: for example, the two layers of the cerebellar cortex.

To quantitatively evaluate the segmentation method, we have created a gold standard segmentation of the public 100-micron brain[12], which we are publicly releasing as part of NextBrain. To make this burdensome task practical and feasible, we simplified it in five manners: (1) downsampling the data to 200-µm resolution, (2) labelling only one hemisphere, (3) using the same semi-automated artificial intelligence method as in NextBrain for faster segmentation, (4) using FreeSurfer to automatically subdivide the cerebral cortex and (5) labelling only a subset of 98 visible ROIs (Supplementary Videos 3 and 4). Even with these simplifications, labelling the scan took more than 100 h of manual tracing effort.

We compared the gold standard labels with the automated segmentations produced by NextBrain using Dice overlap scores. Because the gold standard has fewer ROIs (particularly in the brainstem), we (1) clustered the ROIs in the automated segmentation that correspond with the ROIs in the gold standard and (2) used a version of NextBrain in which the brainstem ROIs are simplified to better match those of the gold standard (with 264 labels instead of 333). The results are shown in Extended Data Table 1. As expected, there is a clear link between size and Dice. Larger ROIs like the cerebral white matter or cortex have Dice around 0.9. The smaller ROIs have lower Dice, but very few are below 0.4—which is enough to localize ROIs. We note that the median Dice (0.667) is comparable with that reported by other Bayesian segmentation methods for brain subregions[38].

Sample slices and their corresponding automated and manual segmentations are shown in Fig. 4. The exquisite resolution and contrast of the dataset enables our atlas to accurately delineate a large number of ROIs with very different sizes, including small nuclei and subregions of the hippocampus, amygdala, thalamus, hypothalamus, midbrain and so on. Differences in label granularity aside, the consistency between the automated and gold standard segmentation is qualitatively very strong.

This is a highly comprehensive dense segmentation of a human brain MRI scan. As ex vivo datasets with tens of scans become available[30,39], https://dandiarchive.org/dandiset/000026, our tool has great potential in augmenting mesoscopic studies of the human brain. Moreover, the labelled MRI that we are releasing has great potential in other neuroimaging studies, for example, for training or evaluating segmentation algorithms; for ROI analysis in the high-resolution ex vivo space; or for volumetric analysis by means of registration-based segmentation.

Fine-grained analysis of in vivo MRI

NextBrain can also be used to automatically segment in vivo MRI scans at the resolution of the atlas (200-µm isotropic), yielding an extremely high level of detail. Scans used in research typically have isotropic resolution with voxel sizes ranging from 0.7 mm to 1.2 mm and therefore do not show all ROI boundaries with as much detail as ultra-high-resolution ex vivo MRI. However, many boundaries are still visible, including the external boundaries of brain structures (hippocampus, thalamus and so on) and some internal boundaries: for example, between the anteromedial and lateral posterior thalamus[40]. Bayesian segmentation capitalizes on these visible boundaries and combines them with the previous knowledge encoded in the atlas to produce the full subdivision—albeit with lower reliability for the indistinct boundaries[10]. A sample segmentation is shown in Fig. 1f.

Evaluation of segmentation accuracy

We first evaluated the in vivo segmentation quantitatively in two different experiments. First, we downsampled the ex vivo MRI scan from the previous section to 1-mm isotropic resolution (that is, the standard resolution of in vivo scans), segmented it at 200-µm resolution and computed Dice scores with the high-resolution reference. The results are displayed in Extended Data Table 1. The median Dice is 0.590, which is 0.077 lower than at 200 µm but still fair for such small ROIs[38]. Moreover, most Dice scores remain over 0.4, as for the ultra-high resolution, hinting that the priors can successfully provide a rough localization of internal boundaries, given the more visible external boundaries.

In a second experiment, we analysed the Dice scores produced by NextBrain in OpenBHB[41], a public meta-dataset with roughly 1-mm isotropic T1-weighted scans of more than 3,000 healthy individuals acquired at more than 60 sites. Using FreeSurfer 7.0 as a silver standard, we computed Dice scores for our segmentations at the level of whole regions: that is, the level of granularity provided by FreeSurfer. Although these scores cannot assess segmentation accuracy at the

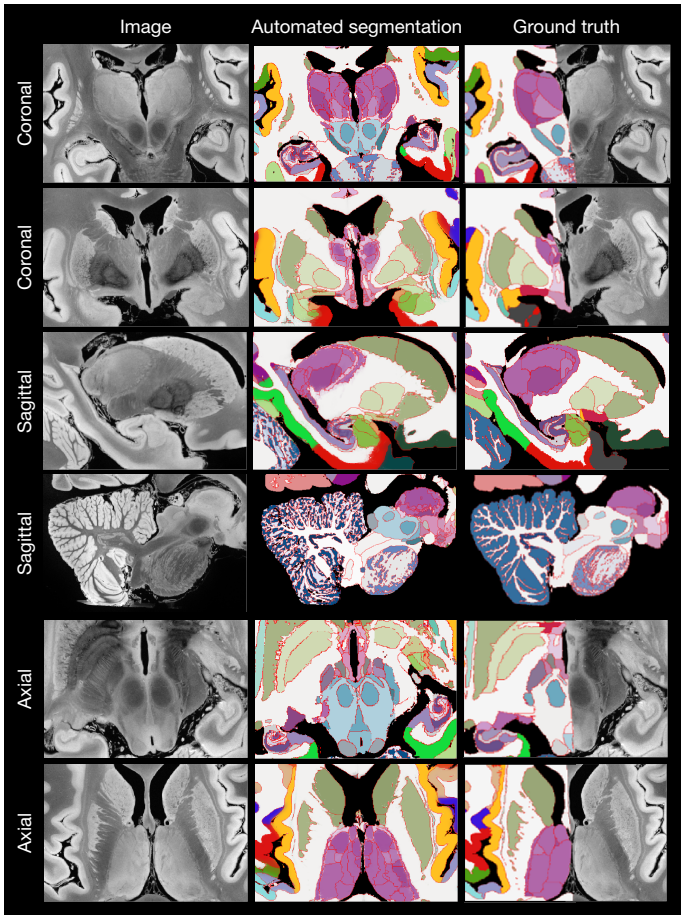

Fig. 4 | NextBrain segmentation of ultra-high-resolution MRI. Automated Bayesian segmentation of publicly available ultra-high-resolution ex vivo brain MRI[12] using the simplified version of NextBrain, and comparison with the gold standard (only available for the right hemisphere). We show two coronal, sagittal and axial slices. The MRI was resampled to 200-µm isotropic resolution for processing. As in previous figures, the segmentation uses the Allen colour map[3] with boundaries overlaid in red. We note that the manual segmentation uses a coarser labelling protocol.

subregion level, they do enable evaluation on a much larger multisite cohort, as well as comparison with the Allen MNI template—the only competing histological (or rather, histology-inspired) atlas that can segment the whole brain in vivo. The results (Extended Data Fig. 6) show that (1) NextBrain consistently outperform the Allen MNI template, as expected from the fact that one atlas is probabilistic whereas the other is not; (2) NextBrain yields Dice scores in the range expected from Bayesian segmentation methods[35]—despite using only five cases, thanks to the excellent generalization ability of generative models[42]; and (3) despite being built from a set of older subjects, our mitigation strategy (anchoring NextBrain on MNI and using highly generalizable Bayesian segmentation) enables NextBrain to produce segmentations that are consistently accurate throughout the lifespan, as opposed to the Allen MNI template, which has a strong negative correlation between age and performance: $r = -0.274$, $P < 10^{-55}$, compared with NextBrain ($r = 0.046$, $P = 0.009$). Please see Extended Data Fig. 6b,c for further details.

Application to Alzheimer's disease classification

To further compare NextBrain with the Allen MNI template, we used an Alzheimer's disease classification task based on linear discriminant analysis (LDA) of ROI volumes (corrected by age and intracranial volume). Using a simple linear classifier on a task where strong differences are expected allows us to use classification accuracy as a proxy for the quality of the input features: that is, the ROI volumes derived from the automated segmentations. To enable direct comparison, we used a sample of 383 subjects from the Alzheimer's Disease Neuroimaging Initiative (ADNI) dataset[43] (168 Alzheimer's disease, 215 controls) that we used in previous publications[10,11,40].

Using the ROI volumes estimated by FreeSurfer 7.0 (which do not include subregions) yields an area under the receiver operating characteristic curve (AUROC) equal to 0.911, with classification accuracy of 85.4% at its elbow. The Allen MNI template exploits subregion information to achieve AUROC = 0.929 and 86.9% accuracy. The increased segmentation accuracy and granularity of NextBrain enables it to achieve AUROC = 0.953 and 90.3% accuracy—with a significant increase in AUROC with respect to the Allen MNI template ($P = 0.01$ for a DeLong test). This AUROC is also higher than those of specific ex vivo atlases we have presented in the previous work[10,11,40]—which range from 0.830 to 0.931.

Application to fine-grained signature of ageing

We performed Bayesian segmentation with NextBrain on 705 subjects (aged 36–90, mean 59.6 years) from the Ageing HCP dataset[44], which comprises high-quality in vivo scans at 0.8-mm resolution. We computed the volumes of the ROIs for every subject, corrected them for total intracranial volume (by division) and sex (by regression) and computed their Spearman correlation with age. We used the Spearman rather than Pearson correlation because, being rank-based, it is a better model for ageing trajectories as they are known to be nonlinear for wide age ranges[45,46].

The result of this analysis is a highly comprehensive map of regional ageing of the human brain (Fig. 5a and Extended Data Fig. 7a; see also full trajectories for select ROIs in Extended Data Fig. 8). Cortically, we found significant negative correlations with age in the prefrontal cortex (marked with 'a' in Fig. 5a) and insula (b), whereas the temporal (c) and parahippocampal cortices (d) did not yield significant correlation; this is consistent with findings from studies of cortical thickness[47,48]. The white matter (e) is known to decline steadily after about 35 years[45,46], and such negative correlation is also detected by NextBrain. Other general ageing patterns at the whole-structure level[45,46] are also successfully captured, such as a steady volume decrease of the caudate, thalamus and putamen (f) and the volumetric reduction of the hippocampus, amygdala and globus pallidus.

Importantly, NextBrain also unveils more granular patterns of the relationship between volumes and ageing in these regions. For example, the anterior caudate (g) showed a stronger negative correlation between age and volume than the posterior caudate (h). Similarly, the external segment of the globus pallidus (i) showed a stronger correlation than the internal segment (j)—an effect that was not observed in previous work studying the whole pallidum[49]. The ability to investigate separate subregions highlights a differential effect of ageing across brain networks, particularly a stronger effect on the regions of the limbic and prefrontal networks, given the correlations we found in the caudate head (g), insula (b), orbitofrontal cortex (k), amygdala and thalamus[50]. In the thalamus, the correlation is more significant in the mediodorsal (l), anteroventral (m) and pulvinar subnuclei (n), key regions in the limbic, lateral orbitofrontal and dorsolateral prefrontal circuits. In the hippocampus, subicular regions (o) correlate more strongly than the rest of the structure. The pattern of correlation strength is more homogeneous across subregions in the amygdala (key region in the limbic system), hypothalamus and cerebellum. We then revisited the OpenBHB dataset and performed the same regression analysis only for subjects older than 35 years, to match the age range of the Ageing HCP dataset ($N = 431$, aged 36–86 years, mean 57.9 years). The results are shown in Fig. 5b and Extended Data Fig. 7b. Despite the differences in acquisition and the huge heterogeneity of the OpenBHB dataset, the results are highly consistent with those from HCP—but with

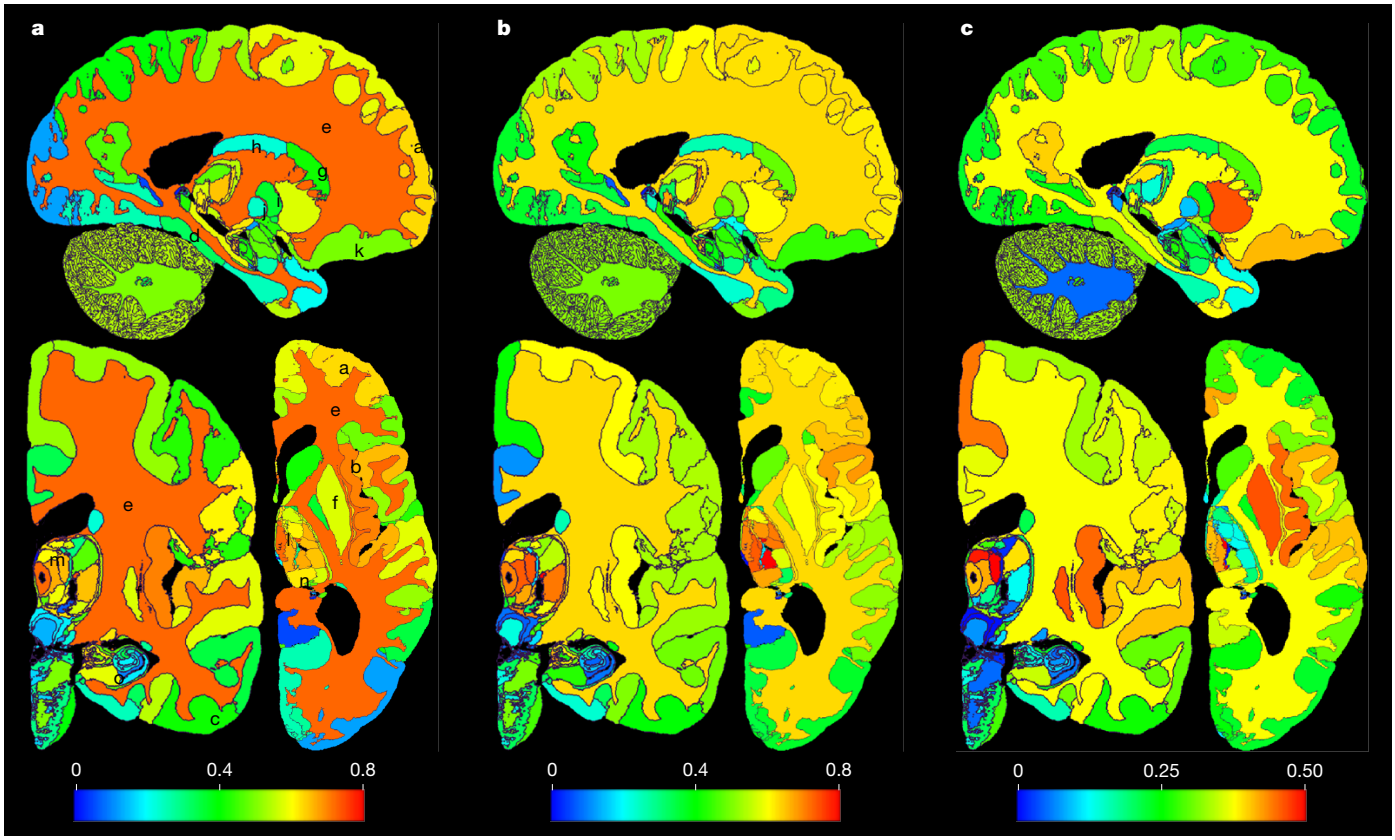

Fig. 5 | Fine-grained ageing signature using NextBrain. We report the absolute value of Spearman correlation for ROI volumes versus age derived from in vivo MRI scans. **a**, Ageing HCP dataset. Image resolution, 0.8-mm isotropic; *N*, 705; age range, 36–90 years; mean age, 59.6 years; please see main text for meaning of markers (letters). **b**, OpenBHB dataset[41], restricted to subjects with ages over 35 years to match Ageing HCP. Resolution, 1-mm isotropic; *N*, 431; age range, 36–86 years; mean age, 57.9 years. **c**, Full OpenBHB dataset. *N*, 3,220; age range, 6–86 years; mean age, 25.2 years; please note the different scale of the colour bar. The ROI volumes are corrected by intracranial volume (by division) and sex (by regression). Further slices are shown in Extended Data Fig. 6.

slightly lower significance, possibly owing to the increased voxel size (twice as big, because $1/0.8^3 \approx 2$).

We also performed the same analysis with all 3,220 subjects in OpenBHB; see the results in Fig. 5c and Extended Data Fig. 7c. For many regions, widening the age range to 6–86 years (mean age 25.2) yields non-monotonic ageing curves and therefore weaker Spearman correlations. Therefore, these graphs highlight the regions whose volumes start decreasing with age the earliest, such as the putamen or medial thalamus. Many other patterns of association between age and ROI volumes remain very similar to those of the older populations (for example, basal ganglia or hippocampus).

The segmentation code is publicly available in FreeSurfer (https://surfer.nmr.mgh.harvard.edu/fswiki/HistoAtlasSegmentation) and can be run with a single line of code. This enables researchers worldwide to analyse their scans at a high level of detail without manual effort or highly specific neuroanatomical knowledge.

Discussion and conclusion

NextBrain is a next-generation probabilistic human brain atlas that is publicly available and distributed with a companion Bayesian segmentation tool and multimodal dataset. The dataset itself is already a highly valuable resource: researchers have free access to both the raw and registered data, which they can use for their own research (for example, in MRI signal modelling or registration) or to augment the atlas with new ROIs (for example, by labelling them on the histology or MRI data and rebuilding the atlas). The atlas itself provides a high-resolution CCF for population analyses. The 3D segmentation of 100-µm ex vivo brain MRI scan[12] is a valuable complement to this (already very useful) resource. Finally, the Bayesian tool enables segmentation of ex vivo and in vivo MRI at an unprecedented level of granularity.

NextBrain is customizable and extensible: because all the data and code are publicly available, it is possible to download the data, modify (or extend) the manual annotations and rebuild a custom atlas. NextBrain can be complemented by other segmentation methods and atlases that describe other aspects of the brain. For example, more accurate cortical segmentation and parcellation can be achieved with surface models[51]. We are at present working on models that combine neural networks with geometry processing to obtain laminar segmentations from in vivo and ex vivo scans[52,53]. Surface placement will also warrant compatibility with cortical atlases obtained with multimodal data[54].

The Bayesian segmentation tool in NextBrain is compatible with 1-mm isotropic scans, as illustrated by the Alzheimer's and ageing experiments. As with other probabilistic atlases, Bayesian segmentation can be augmented with models of pathology to automatically segment pathology, such as tumours[55] or white matter hyperintensities[56]. Importantly, NextBrain's high level of detail enables us to fully take advantage of high-resolution data, such as ex vivo MRI, ultra-high-field MRI (for example, 7 T) and exciting new modalities like HiP-CT[57]. As high-quality 3D brain images become increasingly available, NextBrain's ability to analyse them with high granularity holds great promise to advance knowledge on the human brain in health and in disease.

Online content

Any methods, additional references, Nature Portfolio reporting summaries, source data, extended data, supplementary information,

acknowledgements, peer review information; details of author contributions and competing interests; and statements of data and code availability are available at https://doi.org/10.1038/s41586-025-09708-2.

1. Amunts, K. et al. BigBrain: an ultrahigh-resolution 3D human brain model. *Science* **340**, 1472–1475 (2013).
2. Amunts, K., Mohlberg, H., Bludau, S. & Zilles, K. Julich-Brain: a 3D probabilistic atlas of the human brain's cytoarchitecture. *Science* **369**, 988–992 (2020).
3. Ding, S. L. et al. Comprehensive cellular-resolution atlas of the adult human brain. *J. Comp. Neurol.* **524**, 3127–3481 (2016).
4. Fischl, B. FreeSurfer. *Neuroimage* **62**, 774–781 (2012).
5. Smith, S. M. et al. Advances in functional and structural MR image analysis and implementation as FSL. *Neuroimage* **23**, S208–S219 (2004).
6. Penny, W. D., Friston, K. J., Ashburner, J. T., Kiebel, S. J. & Nichols, T. E. *Statistical Parametric Mapping: The Analysis of Functional Brain Images* (Elsevier, 2011).
7. Fischl, B. et al. Whole brain segmentation: automated labeling of neuroanatomical structures in the human brain. *Neuron* **33**, 341–355 (2002).
8. Rolls, E. T. A computational theory of episodic memory formation in the hippocampus. *Behav. Brain Res.* **215**, 180–196 (2010).
9. Yushkevich, P. A. et al. A high-resolution computational atlas of the human hippocampus from postmortem magnetic resonance imaging at 9.4 T. *Neuroimage* **44**, 385–398 (2009).
10. Iglesias, J. E. et al. A computational atlas of the hippocampal formation using ex vivo, ultra-high resolution MRI: application to adaptive segmentation of in vivo MRI. *Neuroimage* **115**, 117–137 (2015).
11. Saygin, Z. M. et al. High-resolution magnetic resonance imaging reveals nuclei of the human amygdala: manual segmentation to automatic atlas. *Neuroimage* **155**, 370–382 (2017).
12. Edlow, B. L. et al. 7 Tesla MRI of the ex vivo human brain at 100 micron resolution. *Sci. Data* **6**, 244 (2019).
13. Mai, J. K., Majtanik, M. & Paxinos, G. *Atlas of the Human Brain* (Academic, 2015).
14. Pichat, J., Iglesias, J. E., Yousry, T., Ourselin, S. & Modat, M. A survey of methods for 3D histology reconstruction. *Med. Image Anal.* **46**, 73–105 (2018).
15. Mazziotta, J. et al. A probabilistic atlas and reference system for the human brain: International Consortium for Brain Mapping (ICBM). *Philos. Trans. R. Soc. Lond. B Biol. Sci.* **356**, 1293–1322 (2001).
16. Yelnik, J. et al. A three-dimensional, histological and deformable atlas of the human basal ganglia. I. Atlas construction based on immunohistochemical and MRI data. *Neuroimage* **34**, 618–638 (2007).
17. Krauth, A. et al. A mean three-dimensional atlas of the human thalamus: generation from multiple histological data. *Neuroimage* **49**, 2053–2062 (2010).
18. Ashburner, J. & Friston, K. J. Unified segmentation. *Neuroimage* **26**, 839–851 (2005).
19. Paquola, C. et al. The BigBrainWarp toolbox for integration of BigBrain 3D histology with multimodal neuroimaging. *eLife* **10**, e70119 (2021).
20. Alkemade, A. et al. A unified 3D map of microscopic architecture and MRI of the human brain. *Sci. Adv.* **8**, eabj7892 (2022).
21. Sotiras, A., Davatzikos, C. & Paragios, N. Deformable medical image registration: a survey. *IEEE Trans. Med. Imaging* **32**, 1153–1190 (2013).
22. Ferrante, E. & Paragios, N. Slice-to-volume medical image registration: a survey. *Med. Image Anal.* **39**, 101–123 (2017).
23. Mancini, M. et al. Hierarchical joint registration of tissue blocks with soft shape constraints for large-scale histology of the human brain. In *Proc. 16th International Symposium on Biomedical Imaging (ISBI 2019)* 666–669 (IEEE, 2019).
24. Casamitjana, A., Mancini, M. & Iglesias, J. E. Synth-by-reg (sbr): contrastive learning for synthesis-based registration of paired images. In *Proc. Simulation and Synthesis in Medical Imaging: 6th International Workshop, Held in Conjunction with MICCAI 2021* (eds Svoboda, D. et al.) 44–54 (Springer, 2021).
25. Casamitjana, A. et al. Robust joint registration of multiple stains and MRI for multimodal 3D histology reconstruction: application to the Allen human brain atlas. *Med. Image Anal.* **75**, 102265 (2022).
26. Mancini, M. et al. A multimodal computational pipeline for 3D histology of the human brain. *Sci. Rep.* **10**, 13839 (2020).
27. Rohlfing, T. Image similarity and tissue overlaps as surrogates for image registration accuracy: widely used but unreliable. *IEEE Trans. Med. Imaging* **31**, 153–163 (2011).
28. Atzeni, A., Jansen, M., Ourselin, S. & Iglesias, J. E. A probabilistic model combining deep learning and multi-atlas segmentation for semi-automated labelling of histology. In *Proc. Medical Image Computing and Computer Assisted Intervention—MICCAI 2018* (eds Frangi, A. F. et al.) 219–227 (Springer, 2018).
29. Desikan, R. S. et al. An automated labeling system for subdividing the human cerebral cortex on MRI scans into gyral based regions of interest. *Neuroimage* **31**, 968–980 (2006).
30. Khandelwal, P. et al. Automated deep learning segmentation of high-resolution 7 Tesla postmortem MRI for quantitative analysis of structure-pathology correlations in neurodegenerative diseases. *Imaging Neurosci.* **2**, 1–30 (2024).
31. Salehi, P. & Chalechale, A. Pix2pix-based stain-to-stain translation: a solution for robust stain normalization in histopathology images analysis. In *Proc. 2020 International Conference on Machine Vision and Image Processing (MVIP)* 1–7 (IEEE, 2020).
32. Alyami, W., Kyme, A. & Bourne, R. Histological validation of MRI: a review of challenges in registration of imaging and whole-mount histopathology. *J. Magn. Reson. Imaging* **55**, 11–22 (2022).
33. Van Leemput, K. Encoding probabilistic brain atlases using Bayesian inference. *IEEE Trans. Med. Imaging* **28**, 822–837 (2008).
34. Modat, M. et al. Parametric non-rigid registration using a stationary velocity field. In *Proc. 2012 IEEE Workshop on Mathematical Methods in Biomedical Image Analysis* 145–150 (IEEE, 2012).
35. Puonti, O., Iglesias, J. E. & Van Leemput, K. Fast and sequence-adaptive whole-brain segmentation using parametric Bayesian modeling. *NeuroImage* **143**, 235–249 (2016).
36. DeFelipe, J. From the connectome to the synaptome: an epic love story. *Science* **330**, 1198–1201 (2010).
37. Horn, A. et al. Lead-DBS v2: towards a comprehensive pipeline for deep brain stimulation imaging. *Neuroimage* **184**, 293–316 (2019).
38. Van Leemput, K. et al. Automated segmentation of hippocampal subfields from ultra-high resolution in vivo MRI. *Hippocampus* **19**, 549–557 (2009).
39. Costantini, I. et al. A cellular resolution atlas of Broca's area. *Sci. Adv.* **9**, eadg3844 (2023).
40. Iglesias, J. E. et al. A probabilistic atlas of the human thalamic nuclei combining ex vivo MRI and histology. *Neuroimage* **183**, 314–326 (2018).
41. Dufumier, B. et al. OpenBHB: a large-scale multi-site brain MRI data-set for age prediction and debiasing. *Neuroimage* **263**, 119637 (2022).
42. Ng, A. & Jordan, M. On discriminative vs. generative classifiers: a comparison of logistic regression and naive Bayes. In *Proc. 15th International Conference on Neural Information Processing Systems: Natural and Synthetic* (eds Dietterich, T. G. et al.) 841–848 (MIT Press, 2001).
43. Jack, C. R. Jr et al. The Alzheimer's disease neuroimaging initiative (ADNI): MRI methods. *J. Magn. Reson. Imaging* **27**, 685–691 (2008).
44. Bookheimer, S. Y. et al. The lifespan human connectome project in aging: an overview. *Neuroimage* **185**, 335–348 (2019).
45. Coupé, P., Catheline, G., Lanuza, E., Manjón, J. V. & Initiative, A.sD. N. Towards a unified analysis of brain maturation and aging across the entire lifespan: A MRI analysis. *Hum. Brain Mapp.* **38**, 5501–5518 (2017).
46. Billot, B. et al. Robust machine learning segmentation for large-scale analysis of heterogeneous clinical brain MRI datasets. *Proc. Natl Acad. Sci. USA* **120**, e2216399120 (2023).
47. Salat, D. H. et al. Thinning of the cerebral cortex in aging. *Cereb. Cortex* **14**, 721–730 (2004).
48. Llamas-Rodríguez, J. et al. TDP-43 and tau concurrence in the entorhinal subfields in primary age-related tauopathy and preclinical Alzheimer's disease. *Brain Pathol.* **33**, e13159 (2023).
49. Narvacan, K., Treit, S., Camicioli, R., Martin, W. & Beaulieu, C. Evolution of deep gray matter volume across the human lifespan. *Hum. Brain Mapp.* **38**, 3771–3790 (2017).
50. Alexander, G. E., DeLong, M. R. & Strick, P. L. Parallel organization of functionally segregated circuits linking basal ganglia and cortex. *Annu. Rev. Neurosci.* **9**, 357–381 (1986).
51. Fischl, B. & Dale, A. M. Measuring the thickness of the human cerebral cortex from magnetic resonance images. *Proc. Natl Acad. Sci. USA* **97**, 11050–11055 (2000).
52. Gopinath, K. et al. Cortical analysis of heterogeneous clinical brain MRI scans for large-scale neuroimaging studies. In *Proc. Medical Image Computing and Computer Assisted Intervention – MICCAI 2023* (eds Greenspan, H. et al.) 35–45 (Springer Nature, 2023).
53. Zeng, X. et al. Segmentation of supragranular and infragranular layers in ultra-high resolution 7T ex vivo MRI of the human cerebral cortex. *Cereb. Cortex* **34**, bhae362 (2024).
54. Glasser, M. F. et al. A multi-modal parcellation of human cerebral cortex. *Nature* **536**, 171–178 (2016).
55. Prastawa, M., Bullitt, E., Moon, N., Van Leemput, K. & Gerig, G. Automatic brain tumor segmentation by subject specific modification of atlas priors1. *Acad. Radiol.* **10**, 1341–1348 (2003).
56. Cerri, S. et al. A contrast-adaptive method for simultaneous whole-brain and lesion segmentation in multiple sclerosis. *Neuroimage* **225**, 117471 (2021).
57. Walsh, C. et al. Imaging intact human organs with local resolution of cellular structures using hierarchical phase-contrast tomography. *Nat. Methods* **18**, 1532–1541 (2021).

Methods

Brain specimens

Hemispheres from five individuals (including half of the cerebrum, cerebellum and brainstem), were used in this study, following informed consent to use the tissue for research and the ethical approval for research by the National Research Ethics Service Committee London - Central. All hemispheres were fixed in 10% neutral buffered formalin (Fig. 1a). The laterality and demographics are summarized in Supplementary Table 1; the donors were neurologically normal, but one case had an undiagnosed, asymptomatic tumour (diameter roughly 10 mm) in the white matter, adjacent to the pars opercularis. This tumour did not pose issues in any of the processing steps described below.

Data acquisition

Our data acquisition pipeline largely leverages our previous work[26]. We summarize it here for completeness; the reader is referred to the corresponding publication for further details.

MRI scanning. Before dissection, the hemispheres were scanned on a 3-T Siemens MAGNETOM Prisma scanner. The specimens were placed in a container filled with Fluorinert (perfluorocarbon), a proton-free fluid with no MRI signal that yields excellent ex vivo MRI contrast and does not affect downstream histological analysis[58]. The MRI scans were acquired with a T2-weighted sequence (optimized long echo train 3D fast spin echo[59]) with the following parameters: TR = 500 ms, TEeff = 69 ms, BW = 558 hertz per pixel, echo spacing = 4.96 ms, echo train length = 58, 10 averages, with 400-μm isotropic resolution, acquisition time for each average = 547 s, total scanning time = 91 min. These scans were processed with a combination of SAMSEG[35] and the FreeSurfer 7.0 cortical stream[51] to bias-field-correct the images, generate rough subcortical segmentations and obtain white matter and pial surfaces with corresponding parcellations according to the Desikan–Killiany atlas[29] (Fig. 1b).

Dissection. After MRI scanning, each hemisphere is dissected to fit into standard 74 mm × 52 mm cassettes. First, each hemisphere was split into cerebrum, cerebellum and brainstem. Using a metal frame as a guide, these were subsequently cut into 10-mm-thick slices in coronal, sagittal and axial orientation, respectively. These slices were photographed inside a rectangular frame of known dimensions for pixel size and perspective correction; we refer to these images as 'whole slice photographs'. Although the brainstem and cerebellum slices all fit into the cassettes, the cerebrum slices were further cut into as many blocks as needed. 'Blocked slice photographs' were also taken for these blocks (Fig. 1c, left).

Tissue processing and sectioning. After standard tissue processing steps, each tissue block was embedded in paraffin wax and sectioned with a sledge microtome at 25-μm thickness. Before each cut, a photograph was taken with a 24 MPx Nikon D5100 camera (ISO = 100, aperture = f/20, shutter speed = automatic) mounted right above the microtome, pointed perpendicularly to the sectioning plane. These photographs (henceforth 'blockface photographs') were corrected for pixel size and perspective using fiducial markers. The blockface photographs have poor contrast between grey and white matter (Fig. 1c, right) but also negligible nonlinear geometric distortion, so they can be readily stacked into 3D volumes. A two-dimensional convolutional neural network (CNN) pretrained on the ImageNet dataset[60] and fine-tuned on 50 manually labelled examples was used to automatically produce binary tissue masks for the blockface images.

Staining and digitization. We mounted on glass slides and stained two consecutive sections every N (see below), one with H&E and one with LFB (Fig. 1d). The sampling interval was $N = 10$ (that is, 250 μm) for blocks that included subcortical structures in the cerebrum, medial structures of the cerebellum or brainstem structures. The interval was $N = 20$ (500 μm) for all other blocks. All stained sections were digitized with a flatbed scanner at 6,400 DPI resolution (pixel size 3.97 μm). Tissue masks were generated using a two-dimensional CNN similar to the one used for blockface photographs (pretrained on ImageNet and fine-tuned on 100 manually labelled examples).

In vivo ADNI data. The in vivo ADNI dataset used in the preparation of this article were obtained from the ADNI database (https://adni.loni.usc.edu/). The ADNI was launched in 2003 as a public–private partnership, led by Principal Investigator M. W. Weiner. The primary goal of ADNI has been to test whether serial MRI, positron emission tomography, other biological markers and clinical and neuropsychological assessments can be combined to measure the progression of mild cognitive impairment and early Alzheimer's disease. For up-to-date information, see www.adni-info.org.

Dense labelling of histology

Segmentations of 333 ROIs (34 cortical, 299 subcortical) were made by authors E.R., J.A. and E.B. (with guidance from D.K., M.B., Z.J. and J.C.A.) for all the LFB sections, using a combination of manual and automated techniques (Fig. 1e). The general procedure to label each block was (1) produce an accurate segmentation for one of every four sections, (2) run SmartInterpol[28] to automatically segment the sections in between and (3) manually correct these automatically segmented sections when needed. SmartInterpol is a dedicated artificial intelligence technique that we have developed specifically to speed up segmentation of histological stacks in this project.

To obtain accurate segmentations on sparse sections, we used two different strategies depending on the brain region. For the blocks containing subcortical or brainstem structures, ROIs were manually traced from scratch using a combination of ITK-SNAP[61] and FreeSurfer's viewer 'Freeview'. For cerebellum blocks, we first trained a two-dimensional CNN (a U-Net[62]) on 20 sections on which we had manually labelled the white matter and the molecular and granular layers of the cortex. The CNN was then run on the (sparse) sections and the outputs manually corrected. This procedure saves a substantial amount of time, because manually tracing the convoluted shape of the arbor vitae is extremely time consuming. For the cortical cerebrum blocks, we used a similar strategy as for the cerebellum, labelling the tissue as either white or grey matter. The subdivision of the cortical grey matter into parcels was achieved by taking the nearest neighbouring cortical label from the aligned MRI scan (details on the alignment below).

The manual labelling followed neuroanatomical protocols based on different brain atlases, depending on the brain region. Further details on the specific delineation protocols are provided in the Supplementary Information. The general ontology of the 333 ROIs is based on the Allen reference brain[3] and is provide in a spreadsheet as part of the Supplementary Information.

3D histology reconstruction

3D histology reconstruction is the inverse problem of reversing all the distortion that brain tissue undergoes during acquisition, to reassemble a 3D shape that accurately follows the original anatomy. For this purpose, we used a framework with four modules.

Initial blockface alignment. To roughly initialize the 3D reconstruction, we relied on the stacks of blockface photographs. Specifically, we used our previously presented hierarchical joint registration framework[23] that seeks to (1) align each block to the MRI with a similarity transform, by maximizing the normalized cross-correlation of their intensities while (2) discouraging overlap between blocks or gaps in between, by means of a differentiable regularizer. The similarity transforms allowed for rigid deformation (rotation, translation), as well as

isotropic scaling to model the shrinking due to tissue processing. The registration algorithm was initialized with transforms derived from the whole slice, blocked slice and blockface photographs (see details in ref. 26). The registration was hierarchical in the sense that groups of transforms were forced to share the same parameters in the earlier iterations of the optimization, to reflect our knowledge of the cutting procedure. In the first iterations, we clustered the blocks into three groups: cerebrum, cerebellum and brainstem. In the following iterations, we clustered the cerebral blocks that were cut from the same slice and allowed translations in all directions, in-plane rotation and global scaling. In the final iterations, each block alignment was optimized independently. The numerical optimization used the LBFGS algorithm[63]. The approximate average error after this procedure was about 2 mm (ref. 23). A sample 3D reconstruction is shown in Fig. 1f.

Refined alignment with preliminary nonlinear model. Once a good initial alignment is available, we can use the LFB sections to refine the registration. These LFB images have exquisite contrast (Fig. 1d) but suffer from nonlinear distortion—rendering the good initialization from the blockface images crucial. The registration procedure was nearly identical to that of the blockface, with two main differences. First, the similarity term used the local (rather than global) normalized cross-correlation function[64] to handle uneven staining across sections. Second, the deformation model and optimization hierarchy were slightly different because nonlinear registration benefits from more robust methods. Specifically, the first two levels of optimization were the same, with blocks grouped into cerebrum/cerebellum/brainstem (first level) or cerebral slices (second level) and optimization of similarity transforms. The third level (that is, each block independently) was subdivided into four stages in which we optimized transforms with increasing complexity, such that the solution of every level of complexity served as initialization to the next. In the first and simplest stage, we allowed for translations in all directions, in-plane rotation and global scaling (five parameters per block). In the second stage, we added a different scaling parameter in the normal direction of the block (six parameters per block). In the third stage, we allowed for rotation in all directions (eight parameters per block). In the fourth and final stage, we added to every section in every block a nonlinear field modelled with a grid of control points (10-mm spacing) and interpolating B-splines. This final deformation model has about 100,000 parameters per case (about 100 parameters per section, times about 1,000 LFB sections).

Nonlinear artificial intelligence registration. We seek to produce final nonlinear registrations that are accurate, consistent with each other and robust against tears and folds in the sections. We capitalize on Synth-by-Reg (SbR[24]), an artificial intelligence tool for multimodal registration that we have recently developed, to register histological sections to MRI slices resampled to the plane of the histology (as estimated by the linear alignment). SbR exploits the facts that (1) intramodality registration is more accurate than intermodality registration with generic metrics like mutual information[65,66] and (2) there is a correspondence between histological sections and MRI slices: that is, they represent the same anatomy. In short, SbR trains a CNN to make histological sections look like MRI slices (a task known as style transfer[67]), using a second CNN that has been previously trained to register MRI slices to each other. The style transfer relies on the fact that only good MRI synthesis will yield a good match when used as input to the second CNN, which enables SbR to outperform unpaired approaches[24] such as CycleGAN[68]. SbR also includes a contrastive loss[69] that prevents blurring and content shift due to overfitting. SbR produces highly accurate deformations parameterized as stationary velocity fields (SVFs[70]).

Bayesian refinement. Running SbR for each stain and section independently (that is, LFB to resampled MRI and H&E to resampled MRI) yields a reconstruction that is jagged and sensitive to folds and tears. One alternative is to register each histological section to each neighbour directly, which achieves smooth reconstructions but incurs the so-called 'banana effect': that is, a straightening of curved structures[14]. We have proposed a Bayesian method that yields smooth reconstructions without the banana effect[25]. This method follows an overconstrained strategy by computing registrations between LFB and MRI, H&E and MRI, H&E and LFB, each LFB section and the two nearest neighbours in either direction across the stack, each H&E section and its neighbours, and each MRI slice and its neighbours. For a stack with S sections, this procedure yields $15xS\text{-}18$ registrations, whereas the underlying dimensionality of the spanning tree connecting all the images is just $3xS\text{-}1$. We use a probabilistic model of SVFs to infer the most likely spanning tree given the computed registrations, which are seen as noisy measurements of combinations of transforms in the spanning tree. The probabilistic model uses a Laplace distribution, which relies on L1 norms and is thus robust to outliers. Moreover, the properties of SVFs enable us to write the optimization problem as a linear program, which we solve with a standard simplex algorithm[71]. The result of this procedure was a 3D reconstruction that is accurate (it is informed by many registrations), robust and smooth (Figs. 1g and 2).

Atlas construction

The transforms for the LFB sections produced by the 3D reconstructions were applied to the segmentations to bring them into 3D space. Despite the regularizer from ref. 23, minor overlaps and gaps between blocks still occur. The former were resolved by selecting the label that is furthest inside the corresponding ROI. For the latter, we used our previously developed smoothing approach[40].

Given the low number of available cases, we combined the left (2) and right (3) hemispheres into a single atlas. This was achieved by flipping the right hemispheres and computing a probabilistic atlas of the left hemisphere using an iterative technique[33]. To initialize the procedure, we registered the MRI scans to the MNI atlas[15] with the right hemisphere masked out and averaged the deformed segmentations to obtain an initial estimate of the probabilistic atlas. This first registration was based on intensities, using a local normalized cross-correlation loss. From that point on, the algorithm operates exclusively on the segmentations.

Every iteration of the atlas construction process comprises two steps. First, the current estimate of the atlas and the segmentations are coregistered one at a time using (1) a diffeomorphic deformation model based on SVFs parameterized by grids of control points and B-splines (as implemented in NiftyReg[72]), which preserves the topology of the segmentations; (2) a data term, which is the log-likelihood of the label at each voxel according to the probabilities given by the deformed atlas (with a weak Dirichlet prior to prevent logs of zero); and (3) a regularizer based on the bending energy of the field, which encourages regularity in the deformations. The second step of each iteration updates the atlas by averaging the segmentations. The procedure converged (negligible change in the atlas) after five iterations. Slices of the atlas are shown in Figs. 1h and 3.

Bayesian segmentation

Our Bayesian segmentation algorithm builds on well-established methods in the neuroimaging literature[18,73,74]. In short, the algorithm jointly estimates a set of parameters that best explain the observed image in light of the probabilistic atlas, according to a generative model based on a Gaussian mixture model (GMM) conditioned on the segmentation, combined with a model of bias field. The parameters include the deformation of the probabilistic atlas; a set of coefficients describing the bias field; and the means, variances and weights of the GMM. The atlas deformation is regularized in the same way as the atlas construction (bending energy, in our case) and is estimated by means of numerical

optimization with LBFGS. The bias field and GMM parameters are estimated with the Expectation Maximization algorithm[75].

Compared with classical Bayesian segmentation methods operating at 1-mm resolution with just a few classes (for example, SAMSEG[35], SPM[18]), our proposed method has several distinct features:

(1) Because the atlas only describes the left hemisphere, we use a fast deep learning registration method (EasyReg[76]) to register the input scan to MNI space and use the resulting deformation to split the brain into two hemispheres that are processed independently.
(2) Because the atlas only models brain tissue, we run SynthSeg[77] on the input scan to mask out the extracerebral tissue.
(3) Clustering ROIs into tissue types (rather than letting each ROI have its own Gaussian) is particularly important, given the large number of ROIs (333). The user can specify the clustering by means of a configuration file; by default, our public implementation uses a configuration with 15 tissue types, tailored to in vivo MRI segmentation.
(4) The framework is implemented using the PyTorch package, which enables it to run on graphics processing units and curbs segmentation run times to about half an hour per hemisphere.

Sample segmentations with this method can be found in Fig. 1h (in vivo) and Fig. 4 (ex vivo).

Labelling of ultra-high-resolution ex vivo brain MRI

To quantitatively assess the accuracy of our segmentation method on the ultra-high-resolution ex vivo scan, we produced a gold standard segmentation of the publicly available 100-µm scan[12] as follows. First, we downsampled the data to 200-µm resolution and discarded the left hemisphere, to alleviate the manual labelling requirements. Next, we used Freeview to manually label from scratch one coronal slice of every ten; we labelled as many regions from the histological protocol as the MRI contrast allowed—without subdividing the cortex. Then, we used SmartInterpol[28] to complete the segmentation of the missing slices. Next, we manually corrected the SmartInterpol output as needed, until we were satisfied with the 200-µm isotropic segmentation. The cortex was subdivided using standard FreeSurfer routines. This labelling scheme led to a ground truth segmentation with 98 ROIs, which we have made publicly available. Supplementary Videos 3 and 4 fly over the coronal and axial slices of the labelled scan, respectively.

We used a simplified version of the NextBrain atlas when segmenting the 100-µm scan, to better match the ROIs of the automated segmentation and the ground truth (especially in the brainstem). This version was created by replacing the brainstem labels in the histological 3D reconstruction (Fig. 1g, right) by new segmentations made directly in the underlying MRI scan. These segmentations were made with the same methods as for the 100-µm isotropic scan. The new combined segmentations were used to rebuild the atlas.

Automated segmentation with Allen MNI template

Automated labelling with the Allen MNI template relied on registration-based segmentation with the NiftyReg package[34,72], which yields state-of-the-art performance in brain MRI registration[78]. We used the same deformation model and parameters as the NiftyReg authors used in their own registration-based segmentation work[79]: (1) symmetric registration with a deformation model parameterized by a grid of control points (spacing 2.5 mm = 5 voxels) and B-spline interpolation; (2) local normalized cross-correlation as objective function (s.d. 2.5 mm); and (3) bending energy regularization (weight 0.001).

LDA for Alzheimer's disease classification

We performed linear classification of Alzheimer's disease versus controls based on ROI volumes as follows. Leaving out one subject at a time, we used all other subjects to (1) compute linear regression coefficients to correct for sex and age (intracranial volume was corrected by division); (2) estimate mean vectors for the two classes ($\boldsymbol{\mu}_0$, $\boldsymbol{\mu}_1$), as well as a pooled covariance matrix (Σ); and (3) use the means and covariance to compute an unbiased log-likehood criterion L for the left-out subject:

$$L(\mathbf{x}) = (\boldsymbol{\mu}_1 - \boldsymbol{\mu}_0)^t \Sigma^{-1}[\mathbf{x} - 0.5\,(\boldsymbol{\mu}_1 + \boldsymbol{\mu}_0)],$$

where $\mathbf{x}$ is the vector with ICV-, sex- and age-corrected volumes for the left-out subject. Once the criterion L has been computed for all subjects, it can be globally thresholded for accuracy and ROC analysis. We note that, for NextBrain, the high number of ROIs renders the covariance matrix singular. We prevent this by using regularized LDA: we normalize all the ROIs to unit variance and then compute the covariance as $\Sigma = S + \lambda I$, where S is the sample covariance, I is the identity matrix and $\lambda = 1.0$ is a constant. We note that normalizing to unit variance enables us to use a fixed, unit λ—rather than having to estimate λ for every left-out subject.

B-spline fitting of ageing trajectories

To compute the B-spline fits in Extended Data Fig. 8, we first corrected the ROI volumes by sex (using regression) and intracranial volume (by division). Next, we modelled the data with a Laplace distribution, which is robust against outliers which may be caused by potential segmentation mistakes. Specifically, we used an age-dependent Laplacian where the location μ and scale b are both B-splines with four evenly space control points at 30, 51.6, 73.3 and 95 years. The fit is optimized with gradient ascent over the log-likelihood function:

$$L(\theta_\mu, \theta_b) = \sum_{n=1}^{N} \log \mathrm{p}[v_n; \mu(a_n; \theta_\mu), b(a_n; \theta_b)],$$

where $p(x; \mu, b)$ is the Laplace distribution with location μ and scale b; v_n is the volume of ROI for subject n; a_n is the age of subject n; $\mu(a_n; \theta_\mu)$ is a B-spline describing the location, parameterized by θ_μ; and $b(a_n; \theta_b)$ is a B-spline describing the scale, parameterized by θ_b. The 95% confidence interval of the Laplace distribution is given by $\mu \pm 3b$.

Ethics statement

The brain donation programme and protocols have received ethical approval for research by the National Research Ethics Service Committee London - Central, and tissue is stored for research under a license issued by the Human Tissue Authority (no. 12198).

Reporting summary

Further information on research design is available in the Nature Portfolio Reporting Summary linked to this article.

Data availability

The raw data used in this Article (MRI, histology, segmentations and so on) can be downloaded from https://doi.org/10.5522/04/24243835. An online tool to interactively explore the 3D reconstructed data can be found at https://github-pages.ucl.ac.uk/NextBrain. This website also includes links to videos, publications, code and other resources. The segmentation of the ex vivo scan can be found at https://openneuro.org/datasets/ds005422/versions/1.0.1. The databases used in the aging study are freely accessible online: OpenBHB (https://baobablab.github.io/bhb/) and aHCP (https://www.humanconnectome.org/study/hcp-lifespan-aging). The ADNI dataset used in the Alzheimer's disease study is freely accessible with registration at https://adni.loni.usc.edu/data-samples/adni-data/. The atlases used in the Supplementary Information for comparison can be found online: Mai-Paixinos (https://www.thehumanbrain.info/brain/sections.php) and Allen (https://atlas.brain-map.org/).

Code availability

The code used in this Article for 3D histology reconstruction can be downloaded from https://github.com/acasamitjana/ERC_reconstruction and used and distributed freely. The segmentation tool is provided as Python code and is integrated in our neuroimaging toolkit 'FreeSurfer': https://surfer.nmr.mgh.harvard.edu/fswiki/HistoAtlasSegmentation. The source code is available on GitHub: https://github.com/freesurfer/freesurfer/tree/dev/mri_histo_util.

58. Iglesias, J. E. et al. Effect of fluorinert on the histological properties of formalin-fixed human brain tissue. *J. Neuropathol. Exp. Neurol.* **77**, 1085–1090 (2018).
59. Mugler, J. P. III Optimized three-dimensional fast-spin-echo MRI. *J. Magn. Reson. Imaging* **39**, 745–767 (2014).
60. Simonyan, K. & Zisserman, A. Very deep convolutional networks for large-scale image recognition. In *Proc. 3rd International Conference on Learning Representations* 1–14 (ICLR, 2015).
61. Yushkevich, P. A. et al. User-guided 3D active contour segmentation of anatomical structures: significantly improved efficiency and reliability. *Neuroimage* **31**, 1116–1128 (2006).
62. Ronneberger, O., Fischer, P. & Brox, T. U-net: convolutional networks for biomedical image segmentation. In *Proc. 18th International Conference on Medical Image Computing and Computer-Assisted Intervention* (eds Navab, N. et al.) 234–241 (Springer, 2015).
63. Liu, D. C. & Nocedal, J. On the limited memory BFGS method for large scale optimization. *Math. Program.* **45**, 503–528 (1989).
64. Avants, B. B., Epstein, C. L., Grossman, M. & Gee, J. C. Symmetric diffeomorphic image registration with cross-correlation: evaluating automated labeling of elderly and neurodegenerative brain. *Med. Image Anal.* **12**, 26–41 (2008).
65. Iglesias, J. E. et al. Is synthesizing MRI contrast useful for inter-modality analysis? In *Proc. 16th International Conference on Medical Image Computing and Computer-Assisted Intervention* (eds Mori, K. et al.) 631–638 (Springer, 2013).
66. Maes, F., Collignon, A., Vandermeulen, D., Marchal, G. & Suetens, P. Multimodality image registration by maximization of mutual information. *IEEE Trans. Med. Imaging* **16**, 187–198 (1997).
67. Jing, Y. et al. Neural style transfer: a review. *IEEE Trans. Vis. Comput. Graph.* **26**, 3365–3385 (2019).
68. Zhu, J.-Y., Park, T., Isola, P. & Efros, A. A. Unpaired image-to-image translation using cycle-consistent adversarial networks. In *Proc. IEEE International Conference on Computer Vision* 2223–2232 (IEEE, 2017).
69. Chen, T., Kornblith, S., Norouzi, M. & Hinton, G. A simple framework for contrastive learning of visual representations. In *Proc. International Conference on Machine Learning* (eds Daumé, H. & Singh, A.) 1597–1607 (JMLR, 2020).
70. Arsigny, V., Commowick, O., Pennec, X. & Ayache, N. A log-euclidean framework for statistics on diffeomorphisms. In *Proc. 9th Medical Image Computing and Computer-Assisted Intervention – MICCAI 2006* (eds Larsen, R. et al.) 924–931 (Springer, 2006).
71. Boyd, S. P. & Vandenberghe, L. *Convex Optimization* (Cambridge Univ. Press, 2004).
72. Modat, M. et al. Fast free-form deformation using graphics processing units. *Comput. Methods Prog. Biomed.* **98**, 278–284 (2010).
73. Van Leemput, K., Maes, F., Vandermeulen, D. & Suetens, P. Automated model-based tissue classification of MR images of the brain. *IEEE Trans. Med. Imaging* **18**, 897–908 (1999).
74. Wells, W. M., Grimson, W. E. L., Kikinis, R. & Jolesz, F. A. Adaptive segmentation of MRI data. *IEEE Trans. Med. Imaging* **15**, 429–442 (1996).
75. Dempster, A. P., Laird, N. M. & Rubin, D. B. Maximum likelihood from incomplete data via the EM algorithm. *J. R. Stat. Soc. Series B Stat Methodol.* **39**, 1–22 (1977).
76. Iglesias, J. E. A ready-to-use machine learning tool for symmetric multi-modality registration of brain MRI. *Sci. Rep.* **13**, 6657 (2023).
77. Billot, B. et al. SynthSeg: segmentation of brain MRI scans of any contrast and resolution without retraining. *Med. Image Anal.* **86**, 102789 (2023).
78. Klein, A. et al. Evaluation of 14 nonlinear deformation algorithms applied to human brain MRI registration. *Neuroimage* **46**, 786–802 (2009).
79. Cardoso, M. J. et al. Geodesic information flows: spatially-variant graphs and their application to segmentation and fusion. *IEEE Trans. Med. Imaging* **34**, 1976–1988 (2015).

Acknowledgements We would like to thank the donors, without whom this work would have not been possible. We would also like to acknowledge P. Johns for his invaluable courses in neuroanatomy at St George's, University of London. Data collection and sharing for the ADNI data used in this article was funded by the Alzheimer's Disease Neuroimaging Initiative (National Institutes of Health grant no. U01 AG024904) and DOD ADNI (Department of Defense grant no. W81XWH-12-2-0012). ADNI is funded by the National Institute on Aging, the National Institute of Biomedical Imaging and Bioengineering and through generous contributions from the following: AbbVie, Alzheimer's Association; Alzheimer's Drug Discovery Foundation; Araclon Biotech; BioClinica, Inc.; Biogen; Bristol-Myers Squibb Company; CereSpir, Inc.; Cogstate; Eisai Inc.; Elan Pharmaceuticals, Inc.; Eli Lilly and Company; EuroImmun; F. Hoffmann-La Roche Ltd and its affiliated company Genentech, Inc.; Fujirebio; GE Healthcare; IXICO Ltd.; Janssen Alzheimer Immunotherapy Research & Development, LLC.; Johnson & Johnson Pharmaceutical Research & Development LLC.; Lumosity; Lundbeck; Merck & Co., Inc.; Meso Scale Diagnostics, LLC.; NeuroRx Research; Neurotrack Technologies; Novartis Pharmaceuticals Corporation; Pfizer Inc.; Piramal Imaging; Servier; Takeda Pharmaceutical Company; and Transition Therapeutics. The Canadian Institutes of Health Research is providing funds to support ADNI clinical sites in Canada. Private sector contributions are facilitated by the Foundation for the National Institutes of Health (www.fnih.org). The grantee organization is the Northern California Institute for Research and Education, and the study is coordinated by the Alzheimer's Therapeutic Research Institute at the University of Southern California. ADNI data are disseminated by the Laboratory for Neuro Imaging at the University of Southern California. This research has been primarily funded by the European Research Council awarded to J.E.I. (Starting grant no. 677697, project 'BUNGEE-TOOLS'). A.C. is supported by the POSTDOC-UdG203 grant from Universitat de Girona. M.B. is supported by a Fellowship award from the Alzheimer's Society, UK (grant no. AS-JF-19a-004-517). O.P. is supported by a grant from the Lundbeck foundation (grant no. R360–2021–39). M.M. is supported by the Italian National Institute of Health with a Starting Grant and by the Wellcome Trust through a Sir Henry Wellcome Fellowship (grant no. 213722/Z/18/Z). B.L.E. is supported by the Chen Institute MGH Research Scholar Award. Further support was provided by NIH grant nos. 1RF1MH123195, 1R01AG070988, 1UM1MH130981, 1RF1AG080371 and 1R21NS109627.

Author contributions Conceptualization: J.C.A., B.L.E., J.L.H., Z.J., J.E.I. Data curation: A.C., M.M., E.R., J.A., S.C., E.B., B.B., A.A., L.Z., D.L.T., D.K., M.B. Formal analysis: A.C., L.Z., J.E.I. Funding acquisition: J.E.I. Investigation: A.C., M.M., E.R., L.P., R.A., J.A., S.C., E.B., L.Z., J.E.I. Methodology: A.C., M.M., O.P., Y.B., J.L.H., Z.J., J.E.I. Project administration: E.R., J.L.H., C.S., Z.J., J.E.I. Resources: D.L.T., J.L.H., C.S., Z.J. Software: A.C., M.M., B.B., A.A., O.P., Y.B., P.S., J.H., J.E.I. Supervision: E.R., L.P., D.K., M.B., J.L.H., C.S., Z.J., J.E.I. Validation: A.C., J.E.I. Visualization: A.C., P.S., J.H., J.E.I. Writing—original draft: A.C., E.R., J.E.I. Writing—review and editing: all authors.

Competing interests The authors declare no competing interests.

Additional information

Supplementary information The online version contains supplementary material available at https://doi.org/10.1038/s41586-025-09708-2.

Correspondence and requests for materials should be addressed to Juan Eugenio Iglesias.

Peer review information *Nature* thanks Mallar Chakravarty and the other, anonymous, reviewer(s) for their contribution to the peer review of this work. Peer reviewer reports are available.

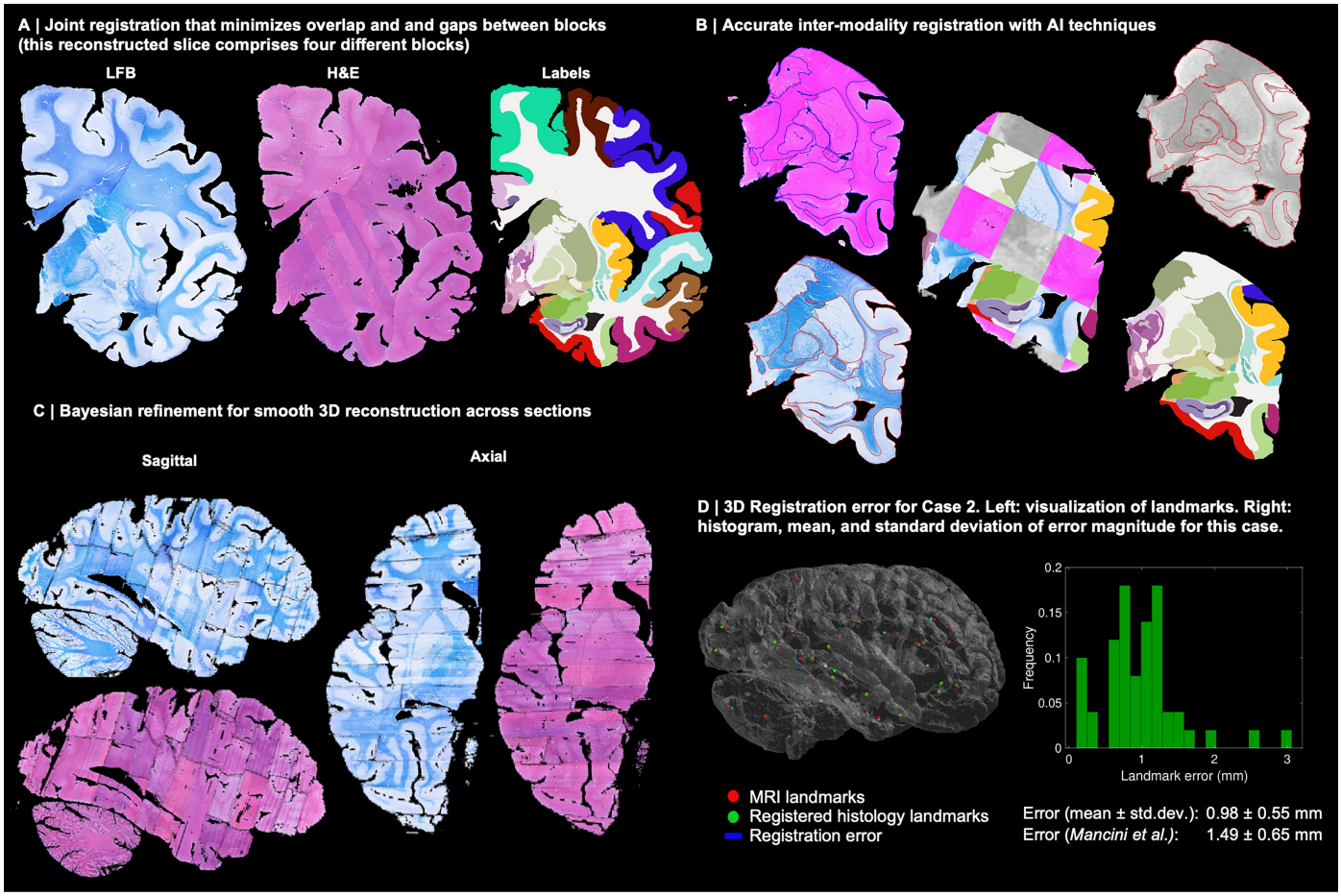

Extended Data Fig. 1 | 3D reconstruction of Case 2. The visualisation follows the same convention as in Fig. 3: (A) Coronal slice of the 3D reconstruction. (B) Registered MRI, LFB, and H&E histology of a block, with tissue boundaries (traced on LFB) overlaid. (C) Orthogonal view of reconstruction, which is smooth and avoids gaps and overlaps. (D) Visualization of 3D landmark registration errors for this specific case (left); histogram of their magnitude (right); and their mean ± standard deviation (bottom), compared with our previous pipeline (Mancini et al.[6]).

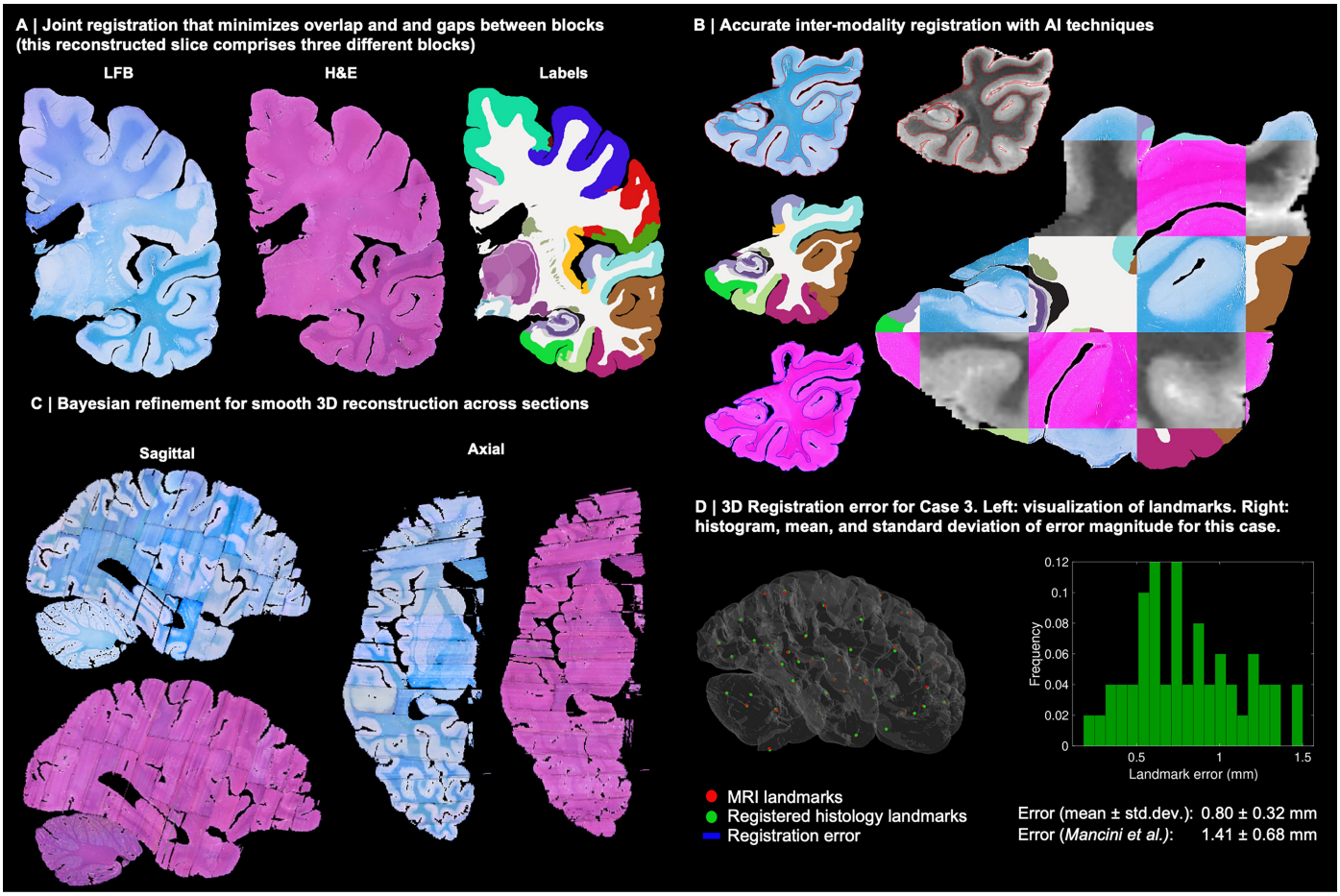

Extended Data Fig. 2 | 3D reconstruction of Case 3. The visualisation follows the same convention as in Fig. 3: (A) Coronal slice of the 3D reconstruction. (B) Registered MRI, LFB, and H&E histology of a block, with tissue boundaries (traced on LFB) overlaid. (C) Orthogonal view of reconstruction, which is smooth and avoids gaps and overlaps. (D) Visualization of 3D landmark registration errors for this specific case (left); histogram of their magnitude (right); and their mean ± standard deviation (bottom), compared with our previous pipeline (Mancini et al.[6]).

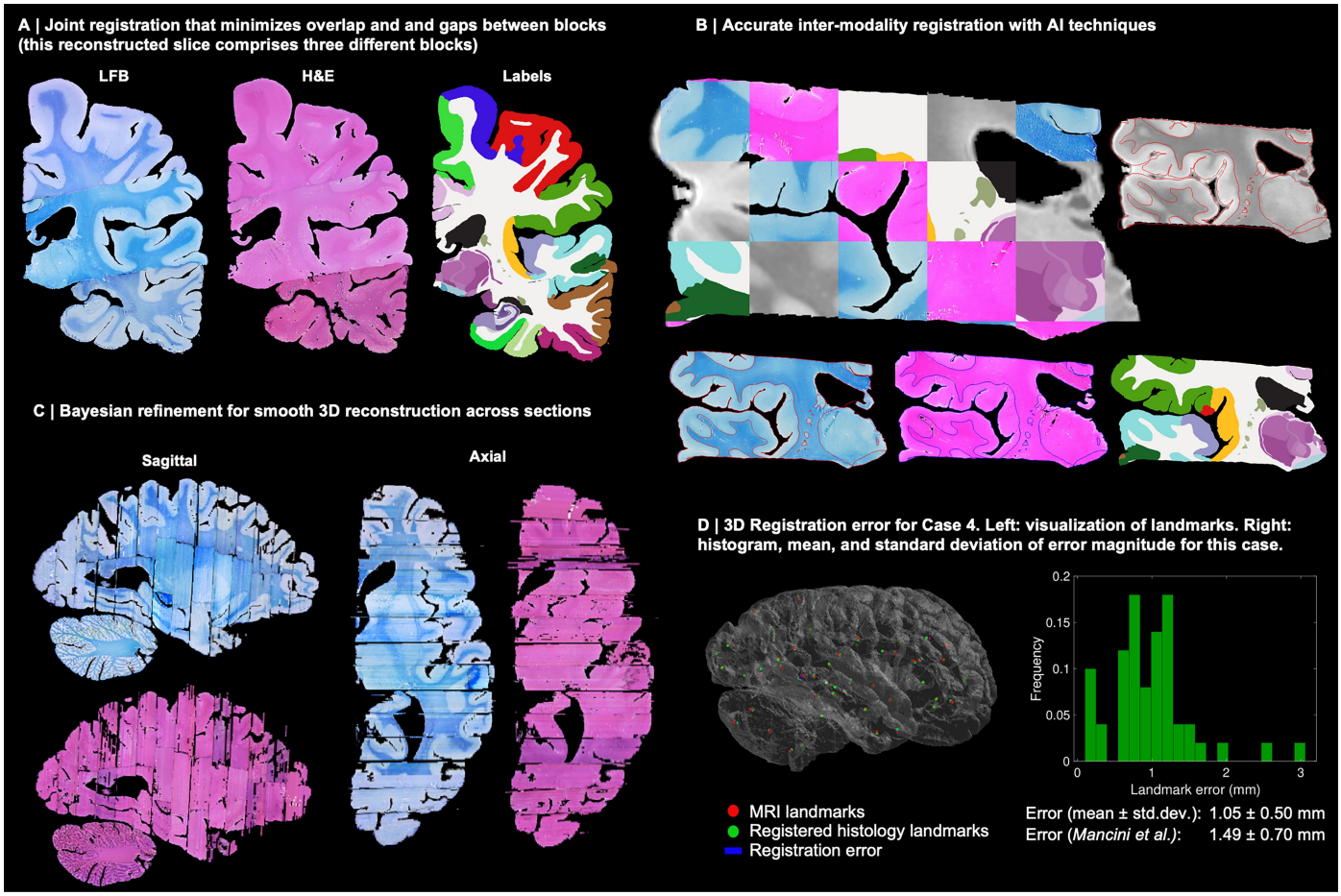

Extended Data Fig. 3 | 3D reconstruction of Case 4. The visualisation follows the same convention as in Fig. 3: (A) Coronal slice of the 3D reconstruction. (B) Registered MRI, LFB, and H&E histology of a block, with tissue boundaries (traced on LFB) overlaid. (C) Orthogonal view of reconstruction, which is smooth and avoids gaps and overlaps. (D) Visualization of 3D landmark registration errors for this specific case (left); histogram of their magnitude (right); and their mean ± standard deviation (bottom), compared with our previous pipeline (Mancini et al.[6]).

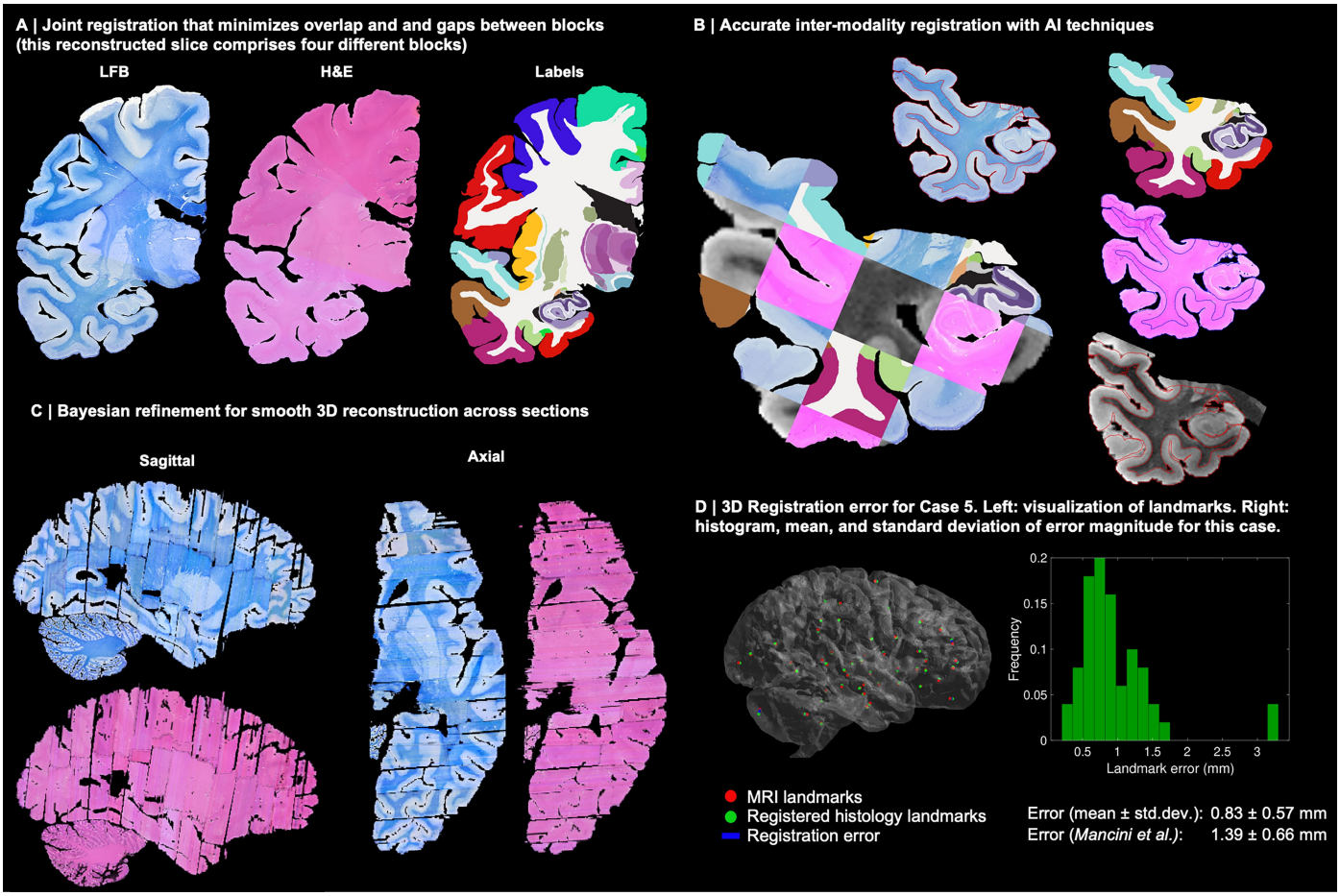

Extended Data Fig. 4 | 3D reconstruction of Case 5. The visualisation follows the same convention as in Fig. 3: (A) Coronal slice of the 3D reconstruction. (B) Registered MRI, LFB, and H&E histology of a block, with tissue boundaries (traced on LFB) overlaid. (C) Orthogonal view of reconstruction, which is smooth and avoids gaps and overlaps. (D) Visualization of 3D landmark registration errors for this specific case (left); histogram of their magnitude (right); and their mean ± standard deviation (bottom), compared with our previous pipeline (Mancini et al.[6]).

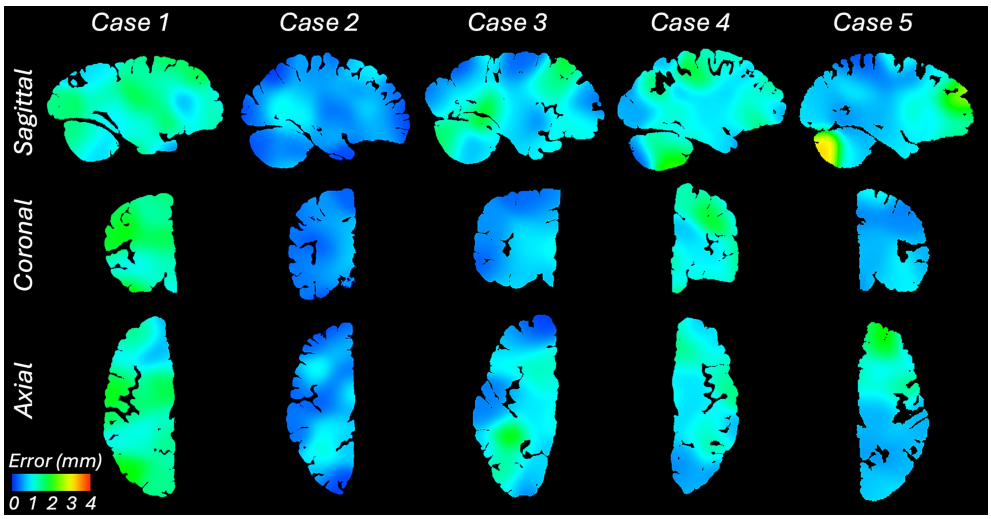

Extended Data Fig. 5 | 3D landmark registration error. Sagittal, coronal, and axial slices of the continuous maps of the 3D landmark registration error. The maps are computed from the discrete landmarks (displayed in Fig. 2d and Extended Data Figs. 1–4d) using Gaussian kernel regression with $\sigma = 10$ mm. There is no clear spatial pattern for the anatomical distribution of the error across subjects.

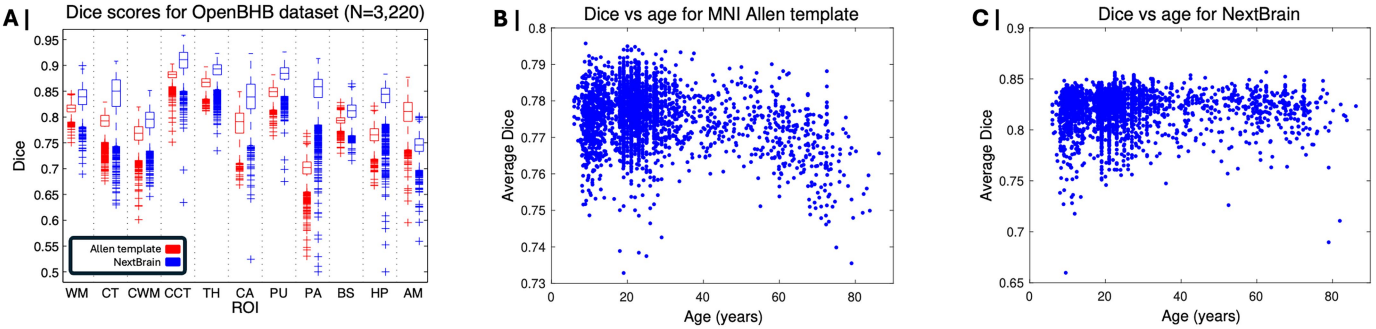

Extended Data Fig. 6 | *NextBrain* superior segmentation performance with respect the Allen MNI template. Dice scores for automated segmentations computed on the OpenBHB dataset (3,330 subjects), using the Allen MNI template and NextBrain, with FreeSurfer segmentations as reference. The scores are computed at the whole regions level, i.e., the level of granularity at which FreeSurfer segments. (A) Box plots for 11 representative ROIs. On each box, the central mark indicates the median, the edges of the box indicate the 25th and 75th percentiles, the whiskers extend to the most extreme data points not considered outliers, and the outliers are plotted individually as '+'. The abbreviations for the regions are: WM = white matter of the cerebrum, CT = cortex of the cerebrum, CWM = cerebellar white matter, CCT = cerebellar cortex, TH = thalamus, CA = caudate, PU = putamen, PA = pallidum, BS = brainstem, HP = hippocampus, AM = amygdala. (B) Scatter plot of Dice (averaged across the same 11 ROIs) vs age for the Allen MNI template. There is a clear negative correlation between age and accuracy: ($r = -0.274$, $p = 1.67 \times 10^{-56}$, two-sided test). (C) Scatter plot for *NextBrain*, whose accuracy is much more consistent across the lifespan, with almost no correlation with age ($r = 0.046$, $p = 0.009$, two-sided test).

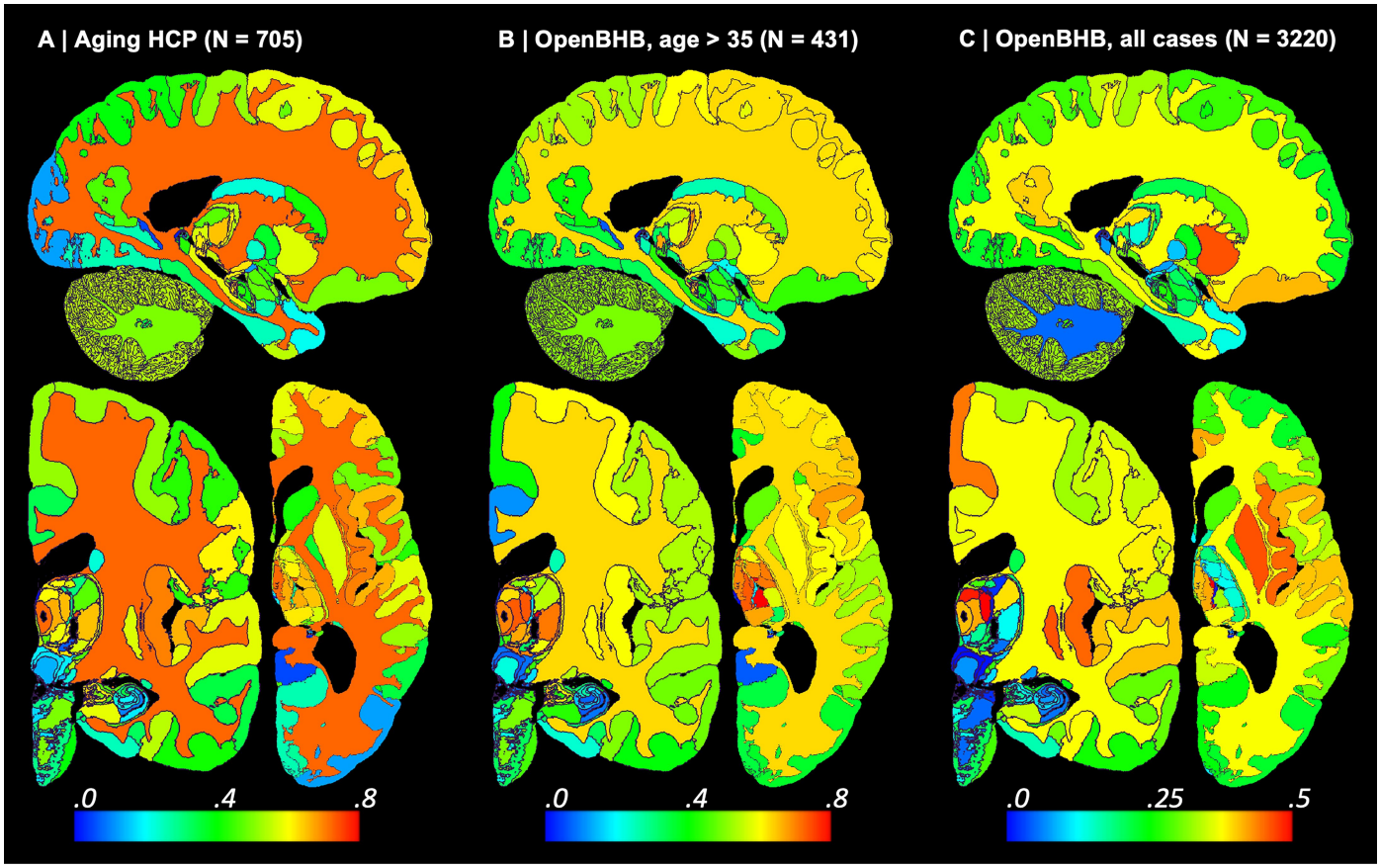

Extended Data Fig. 7 | Fine-grained ageing signature using *NextBrain* (additional slices). We report the absolute value of Spearman correlation for ROI volumes vs age derived from in vivo MRI scans (additional slices). The visualisation follows the same convention as in Fig. 5: (A) Ageing HCP dataset. (B) OpenBHB dataset, restricted to ages over 35. (C) Full OpenBHB dataset.

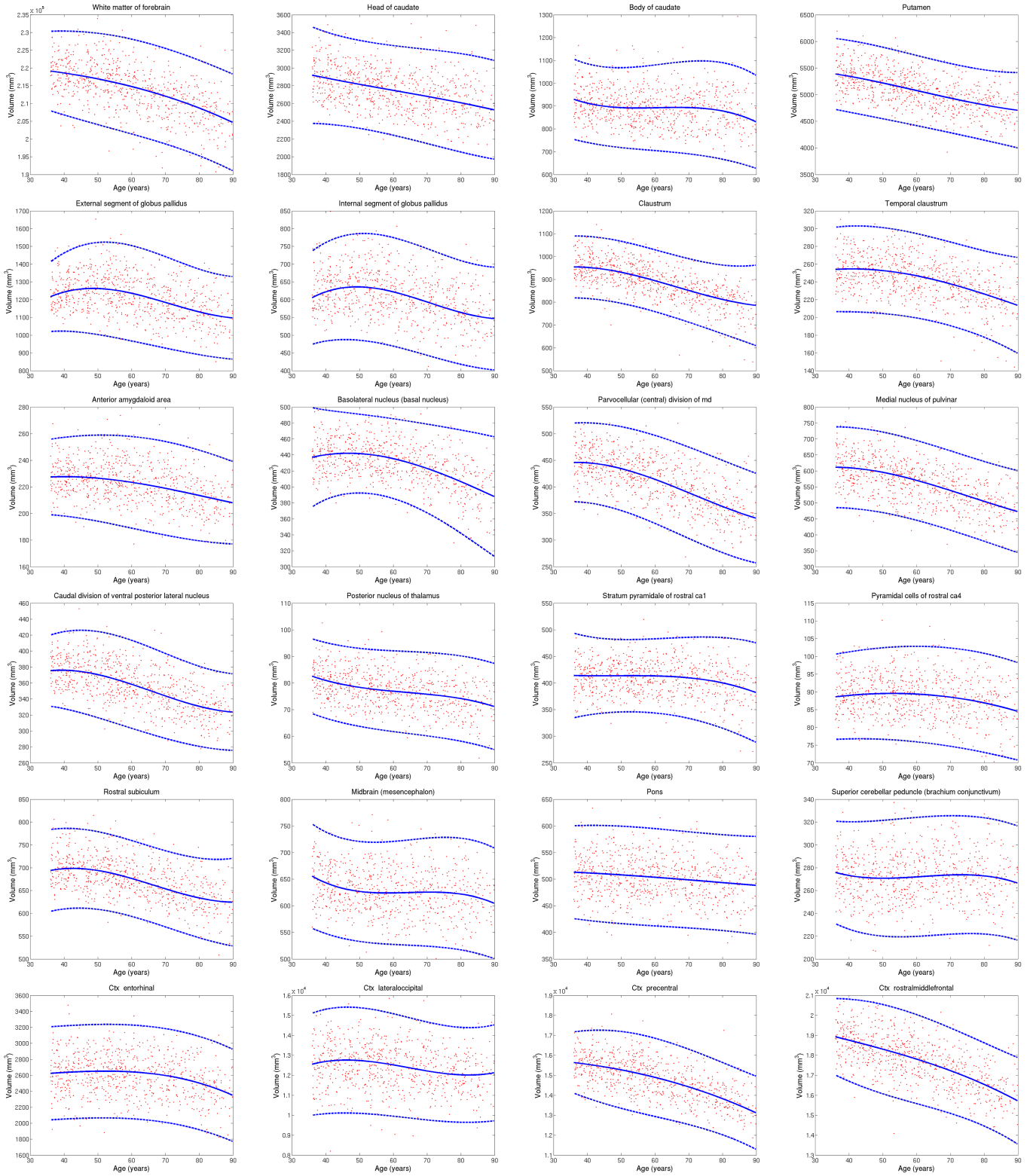

Extended Data Fig. 8 | Ageing trajectories for select ROIs in HCP dataset. Subregions of brain structures (thalamus, hippocampus, cortex, etc) show differential ageing patterns. The red dots correspond to the ROI volumes of individual subjects, corrected by intracranial volume (by division) and sex (by regression). The blue lines represent the maximum likehood fit of a Laplace distribution with location and scale parameters parametrised by a B-spline with four control points (equally space between 30 and 95 years). The continuous blue line represents the location, whereas the dashed lines represent the 95% confidence interval (equal to three times the scale parameter in either direction of the location). Volumes of contralateral structures are averaged across left and right.

Extended Data Table 1 | *NextBrain* segmentation performance on ultra-high resolution ex vivo MRI scan

ROI	Dice (200 µm)	Dice (1 mm)
Cerebral-White-Matter	0.90871	0.81367
Ctx-whole	0.89455	0.81493
Cerebellum-Cortex	0.93205	0.85472
ctx-superiorfrontal	0.77579	0.67069
Cerebellum-White-Matter	0.84393	0.65269
ctx-inferiorparietal	0.77458	0.68367
ctx-precentral	0.73685	0.65937
ctx-rostralmiddlefrontal	0.72036	0.66448
ctx-superiortemporal	0.78506	0.69595
ctx-superiorparietal	0.63853	0.56005
ctx-middletemporal	0.71694	0.67675
ctx-inferiortemporal	0.64805	0.65658
ctx-lateraloccipital	0.61442	0.57929
ctx-postcentral	0.72245	0.60464
ctx-supramarginal	0.78025	0.66091
ctx-precuneus	0.72374	0.61229
ctx-fusiform	0.64278	0.5845
ctx-rh-lateralorbitofrontal	0.69867	0.66915
Brain-Stem	0.65342	0.64177
ctx-insula	0.80767	0.73846
ctx-caudalmiddlefrontal	0.65308	0.52521
ctx-medialorbitofrontal	0.73295	0.62687
ctx-lingual	0.66735	0.59501
ctx-parsopercularis	0.70901	0.63893
Left-Putamen	0.9199	0.86072
ctx-paracentral	0.66197	0.58969
ctx-parstriangularis	0.68932	0.65785
Left-Caudate	0.91102	0.86814
ctx-cuneus	0.56676	0.52349
Pons	0.73371	0.6236
ctx-caudalanteriorcingulate	0.6305	0.56515
ctx-bankssts	0.67939	0.4762
ctx-isthmuscingulate	0.70825	0.55557
ctx-parsorbitalis	0.43236	0.42366
Pons-nuc	0.65229	0.5514
ctx-rh-posteriorcingulate	0.69731	0.56382
ctx-rostralanteriorcingulate	0.67935	0.41073
ctx-pericalcarine	0.5253	0.38703
ctx-entorhinal	0.72093	0.65273
ctx-temporalpole	0.54659	0.49421
ctx-parahippocampal	0.73123	0.66232
Left-PuL	0.76937	0.78917
Left-external-pallidum	0.78074	0.79407
Left-MDl	0.87316	0.86494
ctx-frontalpole	0.11589	0.3493
ctx-transversetemporal	0.63184	0.56123
Left-VA	0.6994	0.73112
CA1	0.78967	0.60729
Fornix	0.30751	0.29593
Claustrum	0.48364	0.3618

ROI	Dice (200 µm)	Dice (1 mm)
Reticular-of-thalamus	0.2386	0.3239
VPL	0.57387	0.62796
LP	0.73933	0.73133
molecular_layer_HP	0.50045	0.50313
Internal-pallidum	0.78939	0.83776
subiculum	0.69842	0.61734
Dentate-cerebellum	0.71523	0.54696
alveus	0.57837	0.3076
CA4_GC-DG	0.75655	0.7136
Accumbens-area	0.77455	0.67541
Thalamus	0.32506	0.32978
Lateral-nucleus	0.8586	0.75999
CeM	0.6668	0.70489
Substancia-Nigra	0.7045	0.63047
CA2_CA3	0.54381	0.4454
AV	0.59365	0.60739
Basal-nucleus	0.66909	0.61273
SCP	0.71921	0.67856
hypothalamus_posterior	0.58318	0.53634
hypothalamus_tubular_sup	0.51626	0.48914
Accessory-Basal-nucleus	0.74887	0.78098
hypothalamus_tubular_inf	0.65529	0.56586
PAG	0.76829	0.7809
Red-Nucleus	0.83407	0.83386
VTA	0.67032	0.4751
STN	0.71496	0.72738
Optic-Nerve	0.58216	0.44427
LGN	0.64318	0.62109
acomm	0.44371	0.42966
fimbria	0.264	0.157
MGN	0.37669	0.21371
VLa	0.32691	0.45109
LD	0.42601	0.46225
stria-terminals	0.50263	0.30588
Central-nucleus-inf-colliculus	0.78275	0.72433
Corticoamygdaloid-transitio	0.58151	0.48352
mammillary_body	0.56602	0.57353
DR	0.54393	0.49046
Inferior-olive	0.26264	0.046102
hypothalamus_anterior_sup	0.54939	0.45936
Medial-nucleus	0.32559	0.33181
Central-nucleus	0.52925	0.48942
Anterior-amygdaloid-area-AAA	0.21345	0.18373
zona-incerta	0.40755	0.45308
hypothalamus_anterior_inf	0.36912	0.32702
Paralaminar-nucleus	0.14105	0.13123
Cortical-nucleus	0.30083	0.23504
Rest of hippocampus	N/A	N/A
Rest of amygdala	N/A	N/A

Dice scores between the ground truth labels of the 100 µm ex vivo brain MRI scan presented in[3] and the automated segmentations obtained with *NextBrain*. ROIs are listed in decreasing order of size (volume). The Dice scores are shown for segmentations obtained at two different resolutions: 200 µm (the resolution at which we created the ground truth labels) and 1 mm (which is representative of in vivo data). We note that the Dice scores are computed from labels made on the right hemisphere (since we did not label the left side of the brain). We also note that the labels "rest of hippocampus" and "rest of amygdala" correspond to voxels that did not clearly belong to any of the manually labelled nuclei, and have therefore no direct correspondence with ROIs in *NextBrain*.

nature portfolio

Corresponding author(s): Juan Eugenio Iglesias

Last updated by author(s): Aug 8, 2025

Reporting Summary

Nature Portfolio wishes to improve the reproducibility of the work that we publish. This form provides structure for consistency and transparency in reporting. For further information on Nature Portfolio policies, see our Editorial Policies and the Editorial Policy Checklist.

Statistics

For all statistical analyses, confirm that the following items are present in the figure legend, table legend, main text, or Methods section.

n/a	Confirmed	
☐	☒	The exact sample size (*n*) for each experimental group/condition, given as a discrete number and unit of measurement
☒	☐	A statement on whether measurements were taken from distinct samples or whether the same sample was measured repeatedly
☐	☒	The statistical test(s) used AND whether they are one- or two-sided *Only common tests should be described solely by name; describe more complex techniques in the Methods section.*
☐	☒	A description of all covariates tested
☐	☒	A description of any assumptions or corrections, such as tests of normality and adjustment for multiple comparisons
☐	☒	A full description of the statistical parameters including central tendency (e.g. means) or other basic estimates (e.g. regression coefficient) AND variation (e.g. standard deviation) or associated estimates of uncertainty (e.g. confidence intervals)
☐	☒	For null hypothesis testing, the test statistic (e.g. *F*, *t*, *r*) with confidence intervals, effect sizes, degrees of freedom and *P* value noted *Give P values as exact values whenever suitable.*
☒	☐	For Bayesian analysis, information on the choice of priors and Markov chain Monte Carlo settings
☒	☐	For hierarchical and complex designs, identification of the appropriate level for tests and full reporting of outcomes
☒	☐	Estimates of effect sizes (e.g. Cohen's *d*, Pearson's *r*), indicating how they were calculated

Our web collection on statistics for biologists contains articles on many of the points above.

Software and code

Policy information about availability of computer code

Data collection	N/A
Data analysis	The code used in this article for 3D histology reconstruc-tion can be downloaded from https://github.com/acasamitjana/ERC_reconstruction and can be used and distributed freely. The segmentation tool is provided as Python code and is integrated in our neuroimaging toolkit"FreeSurfer" (starting at version 8.0): https://surfer.nmr.mgh.harvard.edu/fswiki/HistoAtlasSegmentation. The source code is available on GitHub: https://github.com/freesurfer/freesurfer/tree/dev/mri_histo_util

For manuscripts utilizing custom algorithms or software that are central to the research but not yet described in published literature, software must be made available to editors and reviewers. We strongly encourage code deposition in a community repository (e.g. GitHub). See the Nature Portfolio guidelines for submitting code & software for further information.

Data

Policy information about availability of data

All manuscripts must include a data availability statement. This statement should provide the following information, where applicable:

- Accession codes, unique identifiers, or web links for publicly available datasets
- A description of any restrictions on data availability
- For clinical datasets or third party data, please ensure that the statement adheres to our policy

The raw data used in this article (MRI, histology, delineations, etc.) can be downloaded from:

https://doi.org/10.5522/04/24243835
An online tool to interactively explore the 3D recon-structed data can be found here:
https://github-pages.ucl.ac.uk/NextBrain
This website also includes links to videos, publications, code, and other resources.
The segmentation of the ex vivo scan can be found at: https://openneuro.org/datasets/ds005422/versions/1.0.1
The databases used in the aging study are freely accessible online: OpenBHB (https://baobablab.github.io/bhb/) and aHCP (https://www.humanconnectome.org/study/hcp-lifespan-aging)
The ADNI dataset used in the Alzheimer's disease study is freely accessible with registration in: https://adni.loni.usc.edu/data-samples/adni-data/
The atlases used in the Supplementary Information for comparison can be found online: Mai-Paixinos (https://www.thehumanbrain.info/brain/sections.php) and Allen (https://atlas.brain-map.org/)

Research involving human participants, their data, or biological material

Policy information about studies with human participants or human data. See also policy information about sex, gender (identity/presentation), and sexual orientation and race, ethnicity and racism.

Reporting on sex and gender	Our of the applications of our new atlas that we present in the article is a study of brain atrophy as a function of ageing, using two existing datasets (aHCP and OpenBHB). In these analyses, we consider sex as a covariate, which is standard in volumetric studies of brain regions. Further details on data acquisition and sex determination can be found in the original aHCP and OpenBHB publications.
Reporting on race, ethnicity, or other socially relevant groupings	N/A
Population characteristics	Details on the characteristics of the populations used in our brain ageing study can be found in the original aHCP and OpenBHB publications. Here we used three population subsets: (1) including all N=705 aHCP subjects (aged 36-90, mean 59.6 years), (2) including N=431 OpenBHB subjects (aged 36-86, mean 57.9) and (3) including all N=3220 OpenBHB subjects (aged 6-86, mean=25.2 years). Details on the Alzheimer's disease study can be found on ADNI publications. In our study, we used 383 subjects (168 Alzheimer's disease patients and 215 healthy ageing subjects), aged 56-91, mean 75.8 years.
Recruitment	Again, please see the original aHCP, OpenBHB and ADNI publications.
Ethics oversight	The use of ex vivo tissue was overseen by the National Research Ethics Service (NRES) Committee London-Central.

Note that full information on the approval of the study protocol must also be provided in the manuscript.

Field-specific reporting

Please select the one below that is the best fit for your research. If you are not sure, read the appropriate sections before making your selection.

☒ Life sciences ☐ Behavioural & social sciences ☐ Ecological, evolutionary & environmental sciences

For a reference copy of the document with all sections, see nature.com/documents/nr-reporting-summary-flat.pdf

Life sciences study design

All studies must disclose on these points even when the disclosure is negative.

Sample size	The sample size used in the ageing study was given by the sample size of the original study (aHCP, OpenBHB). The sample size of the Alzheimer's disease study was given to confirm findings in other studies of our group [10, 11, 41]
Data exclusions	No data was excluded from our studies
Replication	Our code and data are publicly available. The OpenBHB and aHCP datasets are publicly available as well.
Randomization	Randomization was not needed as we did not split the sample size into different arms
Blinding	Blinding was not needed as no arms were used in our analyses

Behavioural & social sciences study design

All studies must disclose on these points even when the disclosure is negative.

Study description	*Briefly describe the study type including whether data are quantitative, qualitative, or mixed-methods (e.g. qualitative cross-sectional, quantitative experimental, mixed-methods case study).*

Research sample	*State the research sample (e.g. Harvard university undergraduates, villagers in rural India) and provide relevant demographic information (e.g. age, sex) and indicate whether the sample is representative. Provide a rationale for the study sample chosen. For studies involving existing datasets, please describe the dataset and source.*
Sampling strategy	*Describe the sampling procedure (e.g. random, snowball, stratified, convenience). Describe the statistical methods that were used to predetermine sample size OR if no sample-size calculation was performed, describe how sample sizes were chosen and provide a rationale for why these sample sizes are sufficient. For qualitative data, please indicate whether data saturation was considered, and what criteria were used to decide that no further sampling was needed.*
Data collection	*Provide details about the data collection procedure, including the instruments or devices used to record the data (e.g. pen and paper, computer, eye tracker, video or audio equipment) whether anyone was present besides the participant(s) and the researcher, and whether the researcher was blind to experimental condition and/or the study hypothesis during data collection.*
Timing	*Indicate the start and stop dates of data collection. If there is a gap between collection periods, state the dates for each sample cohort.*
Data exclusions	*If no data were excluded from the analyses, state so OR if data were excluded, provide the exact number of exclusions and the rationale behind them, indicating whether exclusion criteria were pre-established.*
Non-participation	*State how many participants dropped out/declined participation and the reason(s) given OR provide response rate OR state that no participants dropped out/declined participation.*
Randomization	*If participants were not allocated into experimental groups, state so OR describe how participants were allocated to groups, and if allocation was not random, describe how covariates were controlled.*

Ecological, evolutionary & environmental sciences study design

All studies must disclose on these points even when the disclosure is negative.

Study description	*Briefly describe the study. For quantitative data include treatment factors and interactions, design structure (e.g. factorial, nested, hierarchical), nature and number of experimental units and replicates.*
Research sample	*Describe the research sample (e.g. a group of tagged Passer domesticus, all Stenocereus thurberi within Organ Pipe Cactus National Monument), and provide a rationale for the sample choice. When relevant, describe the organism taxa, source, sex, age range and any manipulations. State what population the sample is meant to represent when applicable. For studies involving existing datasets, describe the data and its source.*
Sampling strategy	*Note the sampling procedure. Describe the statistical methods that were used to predetermine sample size OR if no sample-size calculation was performed, describe how sample sizes were chosen and provide a rationale for why these sample sizes are sufficient.*
Data collection	*Describe the data collection procedure, including who recorded the data and how.*
Timing and spatial scale	*Indicate the start and stop dates of data collection, noting the frequency and periodicity of sampling and providing a rationale for these choices. If there is a gap between collection periods, state the dates for each sample cohort. Specify the spatial scale from which the data are taken*
Data exclusions	*If no data were excluded from the analyses, state so OR if data were excluded, describe the exclusions and the rationale behind them, indicating whether exclusion criteria were pre-established.*
Reproducibility	*Describe the measures taken to verify the reproducibility of experimental findings. For each experiment, note whether any attempts to repeat the experiment failed OR state that all attempts to repeat the experiment were successful.*
Randomization	*Describe how samples/organisms/participants were allocated into groups. If allocation was not random, describe how covariates were controlled. If this is not relevant to your study, explain why.*
Blinding	*Describe the extent of blinding used during data acquisition and analysis. If blinding was not possible, describe why OR explain why blinding was not relevant to your study.*

Did the study involve field work? ☐ Yes ☐ No

Field work, collection and transport

Field conditions	*Describe the study conditions for field work, providing relevant parameters (e.g. temperature, rainfall).*
Location	*State the location of the sampling or experiment, providing relevant parameters (e.g. latitude and longitude, elevation, water depth).*
Access & import/export	*Describe the efforts you have made to access habitats and to collect and import/export your samples in a responsible manner and in*

Access & import/export	*compliance with local, national and international laws, noting any permits that were obtained (give the name of the issuing authority, the date of issue, and any identifying information).*
Disturbance	*Describe any disturbance caused by the study and how it was minimized.*

Reporting for specific materials, systems and methods

We require information from authors about some types of materials, experimental systems and methods used in many studies. Here, indicate whether each material, system or method listed is relevant to your study. If you are not sure if a list item applies to your research, read the appropriate section before selecting a response.

Materials & experimental systems

n/a	Involved in the study
☒	☐ Antibodies
☒	☐ Eukaryotic cell lines
☒	☐ Palaeontology and archaeology
☒	☐ Animals and other organisms
☒	☐ Clinical data
☒	☐ Dual use research of concern
☒	☐ Plants

Methods

n/a	Involved in the study
☒	☐ ChIP-seq
☒	☐ Flow cytometry
☐	☒ MRI-based neuroimaging

Antibodies

Antibodies used	*Describe all antibodies used in the study; as applicable, provide supplier name, catalog number, clone name, and lot number.*
Validation	*Describe the validation of each primary antibody for the species and application, noting any validation statements on the manufacturer's website, relevant citations, antibody profiles in online databases, or data provided in the manuscript.*

Eukaryotic cell lines

Policy information about cell lines and Sex and Gender in Research

Cell line source(s)	*State the source of each cell line used and the sex of all primary cell lines and cells derived from human participants or vertebrate models.*
Authentication	*Describe the authentication procedures for each cell line used OR declare that none of the cell lines used were authenticated.*
Mycoplasma contamination	*Confirm that all cell lines tested negative for mycoplasma contamination OR describe the results of the testing for mycoplasma contamination OR declare that the cell lines were not tested for mycoplasma contamination.*
Commonly misidentified lines (See ICLAC register)	*Name any commonly misidentified cell lines used in the study and provide a rationale for their use.*

Palaeontology and Archaeology

Specimen provenance	*Provide provenance information for specimens and describe permits that were obtained for the work (including the name of the issuing authority, the date of issue, and any identifying information). Permits should encompass collection and, where applicable, export.*
Specimen deposition	*Indicate where the specimens have been deposited to permit free access by other researchers.*
Dating methods	*If new dates are provided, describe how they were obtained (e.g. collection, storage, sample pretreatment and measurement), where they were obtained (i.e. lab name), the calibration program and the protocol for quality assurance OR state that no new dates are provided.*

☐ Tick this box to confirm that the raw and calibrated dates are available in the paper or in Supplementary Information.

Ethics oversight	*Identify the organization(s) that approved or provided guidance on the study protocol, OR state that no ethical approval or guidance was required and explain why not.*

Note that full information on the approval of the study protocol must also be provided in the manuscript.

Animals and other research organisms

Policy information about studies involving animals; ARRIVE guidelines recommended for reporting animal research, and Sex and Gender in Research

Laboratory animals	*For laboratory animals, report species, strain and age OR state that the study did not involve laboratory animals.*
Wild animals	*Provide details on animals observed in or captured in the field; report species and age where possible. Describe how animals were caught and transported and what happened to captive animals after the study (if killed, explain why and describe method; if released, say where and when) OR state that the study did not involve wild animals.*
Reporting on sex	*Indicate if findings apply to only one sex; describe whether sex was considered in study design, methods used for assigning sex. Provide data disaggregated for sex where this information has been collected in the source data as appropriate; provide overall numbers in this Reporting Summary. Please state if this information has not been collected. Report sex-based analyses where performed, justify reasons for lack of sex-based analysis.*
Field-collected samples	*For laboratory work with field-collected samples, describe all relevant parameters such as housing, maintenance, temperature, photoperiod and end-of-experiment protocol OR state that the study did not involve samples collected from the field.*
Ethics oversight	*Identify the organization(s) that approved or provided guidance on the study protocol, OR state that no ethical approval or guidance was required and explain why not.*

Note that full information on the approval of the study protocol must also be provided in the manuscript.

Clinical data

Policy information about clinical studies

All manuscripts should comply with the ICMJE guidelines for publication of clinical research and a completed CONSORT checklist must be included with all submissions.

Clinical trial registration	*Provide the trial registration number from ClinicalTrials.gov or an equivalent agency.*
Study protocol	*Note where the full trial protocol can be accessed OR if not available, explain why.*
Data collection	*Describe the settings and locales of data collection, noting the time periods of recruitment and data collection.*
Outcomes	*Describe how you pre-defined primary and secondary outcome measures and how you assessed these measures.*

Dual use research of concern

Policy information about dual use research of concern

Hazards

Could the accidental, deliberate or reckless misuse of agents or technologies generated in the work, or the application of information presented in the manuscript, pose a threat to:

No	Yes	
☐	☐	Public health
☐	☐	National security
☐	☐	Crops and/or livestock
☐	☐	Ecosystems
☐	☐	Any other significant area

Experiments of concern

Does the work involve any of these experiments of concern:

No	Yes	
☐	☐	Demonstrate how to render a vaccine ineffective
☐	☐	Confer resistance to therapeutically useful antibiotics or antiviral agents
☐	☐	Enhance the virulence of a pathogen or render a nonpathogen virulent
☐	☐	Increase transmissibility of a pathogen
☐	☐	Alter the host range of a pathogen
☐	☐	Enable evasion of diagnostic/detection modalities
☐	☐	Enable the weaponization of a biological agent or toxin
☐	☐	Any other potentially harmful combination of experiments and agents

Plants

Seed stocks

Report on the source of all seed stocks or other plant material used. If applicable, state the seed stock centre and catalogue number. If plant specimens were collected from the field, describe the collection location, date and sampling procedures.

Novel plant genotypes

Describe the methods by which all novel plant genotypes were produced. This includes those generated by transgenic approaches, gene editing, chemical/radiation-based mutagenesis and hybridization. For transgenic lines, describe the transformation method, the number of independent lines analyzed and the generation upon which experiments were performed. For gene-edited lines, describe the editor used, the endogenous sequence targeted for editing, the targeting guide RNA sequence (if applicable) and how the editor was applied.

Authentication

Describe any authentication procedures for each seed stock used or novel genotype generated. Describe any experiments used to assess the effect of a mutation and, where applicable, how potential secondary effects (e.g. second site T-DNA insertions, mosiacism, off-target gene editing) were examined.

ChIP-seq

Data deposition

☐ Confirm that both raw and final processed data have been deposited in a public database such as GEO.

☐ Confirm that you have deposited or provided access to graph files (e.g. BED files) for the called peaks.

Data access links
May remain private before publication.

For "Initial submission" or "Revised version" documents, provide reviewer access links. For your "Final submission" document, provide a link to the deposited data.

Files in database submission

Provide a list of all files available in the database submission.

Genome browser session
(e.g. UCSC)

Provide a link to an anonymized genome browser session for "Initial submission" and "Revised version" documents only, to enable peer review. Write "no longer applicable" for "Final submission" documents.

Methodology

Replicates

Describe the experimental replicates, specifying number, type and replicate agreement.

Sequencing depth

Describe the sequencing depth for each experiment, providing the total number of reads, uniquely mapped reads, length of reads and whether they were paired- or single-end.

Antibodies

Describe the antibodies used for the ChIP-seq experiments; as applicable, provide supplier name, catalog number, clone name, and lot number.

Peak calling parameters

Specify the command line program and parameters used for read mapping and peak calling, including the ChIP, control and index files used.

Data quality

Describe the methods used to ensure data quality in full detail, including how many peaks are at FDR 5% and above 5-fold enrichment.

Software

Describe the software used to collect and analyze the ChIP-seq data. For custom code that has been deposited into a community repository, provide accession details.

Flow Cytometry

Plots

Confirm that:

☐ The axis labels state the marker and fluorochrome used (e.g. CD4-FITC).

☐ The axis scales are clearly visible. Include numbers along axes only for bottom left plot of group (a 'group' is an analysis of identical markers).

☐ All plots are contour plots with outliers or pseudocolor plots.

☐ A numerical value for number of cells or percentage (with statistics) is provided.

Methodology

Sample preparation	*Describe the sample preparation, detailing the biological source of the cells and any tissue processing steps used.*
Instrument	*Identify the instrument used for data collection, specifying make and model number.*
Software	*Describe the software used to collect and analyze the flow cytometry data. For custom code that has been deposited into a community repository, provide accession details.*
Cell population abundance	*Describe the abundance of the relevant cell populations within post-sort fractions, providing details on the purity of the samples and how it was determined.*
Gating strategy	*Describe the gating strategy used for all relevant experiments, specifying the preliminary FSC/SSC gates of the starting cell population, indicating where boundaries between "positive" and "negative" staining cell populations are defined.*

☐ Tick this box to confirm that a figure exemplifying the gating strategy is provided in the Supplementary Information.

Magnetic resonance imaging

Experimental design

Design type	N/A (structural MRI only)
Design specifications	N/A
Behavioral performance measures	N/A

Acquisition

Imaging type(s)	structural
Field strength	1.5T-3T (OpenBHB); 3T (aHCP); 3T (ex vivo acquisition)
Sequence & imaging parameters	- OpenBHB: variable. - aHCP: 3D MPRAGE, TR=2400, TE=2.14i, TI=1000, flip=8deg, BW=210Hz/Px iPAT=2. -Ex vivo: T2-weighted sequence (optimised long echo train 3D fast spin echo), TR = 500, TEeff = 69, BW = 558 Hz/Px, echo spacing = 4.96ms, echo train length = 58
Area of acquisition	whole brain

Diffusion MRI ☐ Used ☒ Not used

Preprocessing

Preprocessing software	FreeSurfer 7.0 was used for: 1. cortical parcellation with the Desikan-Killiany atlas; and 2. whole brain segmentation of aHCP and OpenBHB for use as silver standard in the evaluation of segmentation methods.
Normalization	N/A
Normalization template	N/A
Noise and artifact removal	N/A
Volume censoring	N/A

Statistical modeling & inference

Model type and settings	N/A
Effect(s) tested	Effect of aging

Specify type of analysis: ☐ Whole brain ☒ ROI-based ☐ Both

Statistic type for inference (See Eklund et al. 2016)	Spearman correlation for volumes of ROIs
Correction	N/A

Models & analysis

n/a	Involved in the study
☒	☐ Functional and/or effective connectivity
☒	☐ Graph analysis
☒	☐ Multivariate modeling or predictive analysis

Functional and/or effective connectivity	*Report the measures of dependence used and the model details (e.g. Pearson correlation, partial correlation, mutual information).*
Graph analysis	*Report the dependent variable and connectivity measure, specifying weighted graph or binarized graph, subject- or group-level, and the global and/or node summaries used (e.g. clustering coefficient, efficiency, etc.).*
Multivariate modeling and predictive analysis	*Specify independent variables, features extraction and dimension reduction, model, training and evaluation metrics.*